Research Square

Preprints are preliminary reports that have not undergone peer review.
They should not be considered conclusive, used to inform clinical practice,
or referenced by the media as validated information.

Fluorine-Free Superhydrophobic $BiFeO_3$@g-C_3N_4/TEOS-PDMS Cotton Fabric with Magnetic Recoverability for Oil–Water Separation and Z-Scheme Photocatalytic Dye Degradation

Agah Oktay Özdemir

agahoktay58@gmail.com

Erzincan Binali Yıldırım University https://orcid.org/0000-0003-4488-746X

Bülent Çağlar

Ondokuz Mayıs University https://orcid.org/0000-0002-6087-3685

Research Article

Keywords: Superhydrophobic cotton fabric, $BiFeO_3$@g-C_3N_4 nanocomposite, photocatalysis, Oil-water separation, Magnetic responsiveness, Fluorine-free coating

Posted Date: August 12th, 2026

DOI: https://doi.org/10.21203/rs.3.rs-10656285/v1

License: This work is licensed under a Creative Commons Attribution 4.0 International License.
Read Full License

Additional Declarations: The authors declare no competing interests.

Fluorine-Free Superhydrophobic $BiFeO_3$@g-C_3N_4/TEOS-PDMS Cotton Fabric with Magnetic Recoverability for Oil–Water Separation and Z-Scheme Photocatalytic Dye Degradation

Agah Oktay Özdemir [1], Bülent Çağlar [2]

[1]Department of Design, Vocational School, Erzincan Binali Yıldırım University, Erzincan, Türkiye

ORCID: 0000-0003-4488- 746X

[2]Department of Food, Feed and Medicine, Institute of Hemp Research, Ondokuz Mayıs University, Samsun, Türkiye

ORCID:0000-0002-6087-3685

✉ **Corresponding author: Agah Oktay Özdemir agahoktay58@gmail.com**

Abstract: In this study, a fluorine-free, eco-friendly $BiFeO_3$@g-C_3N_4/TEOS-PDMS hybrid-coated smart cotton fabric was successfully developed via an integrated sol-gel and dip-coating approach for multifunctional environmental remediation. Comprehensive structural, morphological, and spectroscopic analyzes (XRD, FTIR, SEM-EDX, XPS, VSM, and DRS) confirmed the uniform anchoring of the magnetic perovskite $BiFeO_3$ and g-C_3N_4 nanocomposite onto the cellulosic fibers through a cross-linked siloxane network. The modified fabric exhibits exceptional superhydrophobic/superoleophilic wettability with water contact angles exceeding 165°, outstanding mechanical durability against abrasion, and a gravity-driven oil-water separation efficiency greater than 99% for both light and heavy organic solvents. Furthermore, the embedded ferromagnetic $BiFeO_3$ nanoparticles enable remotely controllable active oil collection under an external magnetic field. Under UVA and visible-light irradiation, the hybrid textile achieves superior Rhodamine B degradation efficiencies of 77% and 83%, respectively, driven by a direct Z-scheme charge-transfer mechanism that effectively preserves strong redox potentials while simultaneously generating superoxide and hydroxyl radicals. The multifunctional platform maintains high stability, structural integrity, and reusability over 10 consecutive separation cycles and 5 photocatalytic cycles, offering a sustainable and versatile approach for industrial wastewater treatment and oil spill cleanup.

Keywords: Superhydrophobic cotton fabric, $BiFeO_3$@g-C_3N_4 nanocomposite, photocatalysis, Oil-water separation, Magnetic responsiveness, Fluorine-free coating

1. Introduction

With the acceleration of global industrialisation, the textile dyeing industry and the petrochemical industry have emerged as the primary sources of pollution threatening water resources. It is estimated that approximately 10–15% of the dyes used in textile finishing facilities fail to bind to fibers and are discharged directly into wastewater; it is further reported that 40,000–50,000 metric tons of dyes reach aquatic systems annually, and that the textile sector is responsible for approximately 20% of global industrial water pollution (Kavitha et al. 2025). Conversely, oil pollution resulting from maritime accidents, drilling platform leaks, and industrial discharges is causing permanent damage to hydrosphere ecosystems, biodiversity, and drinking water sources (Keramea et al. 2026). Conventional treatment methodologies, including coagulation-flocculation, membrane filtration, activated carbon adsorption, ozonation, and biological treatment, are inadequate for providing a sustainable solution to these pollution problems. This is due to high energy consumption, low removal efficiency, and the production of secondary waste (Ennadi et al. 2026). This situation necessitates the development of solar-powered, fluorine-free, and multifunctional advanced material platforms that can replace fossil-fuel-dependent and waste-intensive treatment technologies (Zhao G et al. 2026). Indeed, contemporary green chemistry principles adopt, as a precondition, the minimization of hazardous substance use, the preference for renewable energy sources, and the design of reusable, multifunctional materials in lieu of single-use systems (Kurul et al. 2025).

Solar-powered photocatalysis for the removal of organic dyes and industrial pollutants is recognized as an environmentally friendly approach that stands out among advanced oxidation technologies due to its use of

renewable energy, full mineralization capacity, and the fact that it does not produce secondary waste (Sak et al. 2026). However, TiO_2, the reference photocatalyst in this field, has a wide bandgap of ~3.2 eV, which allows activation only by UV radiation; this narrow window, comprising only 5% of the solar spectrum, severely limits practical solar energy utilisation efficiency (El Mchaouri et al. 2025; Özdemir 2026). Indeed, in our previous study, we demonstrated that the photocatalytic performance of TiO_2-coated cotton fabric under visible light is significantly enhanced by the sensitisation effect of the dye (Özdemir et al. 2022). This finding has motivated a more in-depth investigation into the potential of narrow-bandgap photocatalysts capable of directly absorbing visible light for textile applications. In this context, bismuth ferrite ($BiFeO_3$), a magnetic perovskite, is attracting increasing interest among multifunctional photocatalysts due to its narrow optical bandgap of 2.0–2.2 eV, strong visible light absorption, inherent ferroelectric polarisation, and magnetic character (Caglar et al. 2021a; Jalandhara et al. 2025). The ferromagnetic structure of $BiFeO_3$ has been shown to enhance its practical application potential by enabling the catalyst to be easily recovered and directed from the reaction medium using an external magnetic field (Chauhan et al. 2025). Meanwhile, graphitic carbon nitride (g-C_3N_4) has emerged as one of the most extensively studied materials among visible-light-active photocatalysts. This is attributable to its π-conjugated polymeric structure, ~2.7 eV bandgap, high chemical and thermal stability, metal-free composition, and ease of synthesis from low-cost precursors such as melamine (Huang et al. 2023). Furthermore, when utilized as single-component materials, both exhibit common limitations such as high photo-generated charge carrier recombination rates, limited reactive oxygen species (ROS) production capacity, and low surface area (Esmaili-Nasrabadi et al. 2026; Zhang et al. 2026). In order to address these shortcomings, heterojunction structures obtained by combining $BiFeO_3$ and g-C_3N_4 components are increasingly being reported in the literature as a synergistic approach that accelerates charge separation, enhances ROS production, and optimises visible-light utilisation efficiency (Katsina et al. 2023; Si et al. 2018).

The design of composite photocatalysts has emerged as the most effective strategy developed to overcome the problem of high charge carrier recombination arising from single-component semiconductors (Wang et al. 2021; Samarasinghe et al. 2025). In conventional Type-II heterojunction structures, the spatial separation of photo-generated electrons and holes is accomplished through the stepwise alignment of the conduction and valence bands of the two semiconductors. Nevertheless, the remaining active band positions in this mechanism may prove thermodynamically insufficient to meet the reduction potential of $O_2/{\bullet}O_2^-$ (−0.33 eV vs. NHE) and the oxidation potential of $\bullet OH/OH^-$ (+1.99 eV vs. NHE); consequently, charge separation occurs at the expense of redox capacity (Samarasinghe et al. 2025; Noureen et al. 2023). In contrast, the Direct Z-Scheme mechanism, inspired by the photosynthesis process in nature, offers a superior charge transfer architecture that fundamentally overcomes this thermodynamic contradiction: in the Z-Scheme, relatively weak electrons in the conduction band of one semiconductor undergo controlled recombination with holes in the valence band of the other semiconductor via the interface. This "controlled sacrifice" ensures that the strongly reducing conduction band and the strongly oxidising valence band remain active simultaneously (Wang et al. 2026; Hu et al. 2024; Jia et al. 2023). As demonstrated in this study, the g-C_3N_4 conduction band (−0.78 eV vs. NHE) facilitates robust ${\bullet}O_2^-$ production, while the $BiFeO_3$ valence band (+2.80 eV vs. NHE) offers considerable •OH production potential. The concurrent production of these two highly reactive oxygen species is consistent only with the Z-scheme architecture, and scavenger experiments targeting reactive radical species are widely accepted as a means of experimentally verifying this (Yi et al. 2024; Zhang C et al. 2025).

In recent years, there has been a significant increase in research interest in superhydrophobic surfaces inspired by biomimetic surfaces found in nature, such as lotus leaves, water spider legs, and rice leaves. These surfaces have attracted considerable attention due to their exceptional water-repellent properties, characterised by a water contact angle exceeding 150° (Wang et al. 2025). The two fundamental design criteria for superhydrophobicity are as follows: the presence of chemical groups with low surface energy and hierarchical micro-/nano-scale structural roughness. The simultaneous fulfilment of these two conditions allows water droplets to remain on the surface in the Cassie-Baxter wetting regime and to roll off easily with minimal adhesion force (Scheff et al. 2025; Guo et al. 2016; Wang et al. 2025). Cotton fabrics represent an exceptionally appealing substrate for superhydrophobic functionalisation, owing to their inherent characteristics such as natural porosity, biodegradability, substantial surface area, mechanical flexibility, and cost-effectiveness (Deng et al. 2020; Abou Elmaaty et al. 2022; Abtew et al. 2026). Nevertheless, contemporary superhydrophobic textile systems are characterised by several critical limitations. A substantial proportion of the extant literature employs fluorinated hydrophobic agents, including per- and polyfluoroalkyl compounds (PFAS). These chemicals present significant environmental and health concerns due to bioaccumulation and ecotoxicity (Pervez et al. 2025). The European Chemicals Agency (ECHA) has classified these compounds as "extremely persistent", and they are subject to increasingly stringent regulatory

restrictions on a global scale (ECHA 2023; Pervez et al. 2025). Conversely, in alternative systems devoid of fluorinated components, concerns persist regarding inadequate wash resistance, diminished stability due to alkaline hydrolysis in high-pH environments, and vulnerability to mechanical wear, which remain the principal challenges in this area (Abu Bakar et al. 2024; Liang et al. 2026; Qin et al. 2023). In this context, tetraethyl orthosilicate (TEOS) and polydimethylsiloxane (PDMS)-based sol-gel coatings emerge as a promising platform for the production of superhydrophobic textiles. This is due to their low surface energy, cross-linked siloxane network, and fluorine-free composition (Abu Bakar et al. 2024; Hadhri et al. 2026; Liu et al. 2024). The most critical limitation, however, is functional singularity: the vast majority of existing superhydrophobic textile systems are limited to water-repellency and self-cleaning functions; integrated platform designs incorporating additional environmental functions -- such as the degradation of organic pollutants, magnetic guidance, and highly efficient oil-water separation -- are extremely rare (Xiang et al. 2022; Rao et al. 2026).

The utilisation of gravity-driven oil-water separation as a filtration strategy for the remediation of industrial oil contamination is becoming increasingly prevalent. This approach is notable for its independence from external energy sources, its cost-effectiveness, and its capacity for scalability (Hu et al. 2025; Maggay et al. 2021). The fundamental functional component of this separation is formed by superhydrophobic/superoleophilic surfaces, which effectively block the water phase via a stable air barrier while selectively allowing the oil phase to pass through due to capillary forces and surface affinity (Rasouli et al. 2021; Hu et al. 2025). Cotton fabrics, with their naturally porous fiber network structure and biodegradability, serve as an ideal substrate that offers bidirectional and highly efficient filtration for both water-heavier and water-lighter oil types (Ren et al. 2026; Zhang Y et al. 2025). In order to overcome the practical limitations of stationary filtration systems, the integration of magnetic guidance capabilities into the system has attracted growing research interest in recent years. While it has been demonstrated in the literature that superhydrophobic textiles containing magnetic nanoparticles can selectively collect the floating oil phase when directed using an external magnetic field, no system has yet been reported that combines this concept with simultaneous photocatalytic activity and superhydrophobicity on an environmentally friendly textile platform (Fu et al. 2018; Riabchykov et al. 2024). The ferromagnetic nature of $BiFeO_3$ nanoparticles provides a unique and distinctive dimension to the developed hybrid system, enabling it to simultaneously achieve both remotely controllable active oil collection and photocatalytic degradation capabilities.

A comprehensive evaluation of the extant literature reveals a preponderance of single-function system designs. The majority of studies on superhydrophobic textiles are oriented towards wash and mechanical durability, while the potential of photocatalysis is largely overlooked. Conversely, studies that are focused on photocatalysis are often divorced from practical textile applications and real-world contamination scenarios. In particular, no comprehensive system design has yet been reported in the literature that simultaneously offers effective visible-light-driven Z-scheme photocatalysis, highly efficient bidirectional oil-water separation, ferromagnetic guidance, and stable superhydrophobic/superoleophilic surface properties on a single fluorine-free textile platform. In this study, a Z-scheme nanocomposite formed by magnetic $BiFeO_3$ perovskite nanoparticles and g-C_3N_4, applied to a cotton fabric surface via a TEOS-PDMS siloxane matrix, was systematically investigated using comprehensive spectroscopic, morphological, and magnetic characterization techniques. The developed system integrates superior superhydrophobic/superoleophilic properties, highly efficient photocatalytic degradation under visible light, potent reactive oxygen species (ROS) generation via a direct Z-scheme mechanism, gravity-driven oil-water separation efficiency exceeding 99%, and ferromagnetically guidable active oil-collection capacity, all within a single environmentally friendly platform. The integration of these functions, as outlined in this study, offers a unique contribution to the field of multifunctional smart textile surfaces.

2. Materials and Methods

2.1. Materials

The materials employed in the synthesis and coating processes comprised 3/1 twill denim fabric, composed of 100% cotton, bleached and washed, with a weight of 300 g/m². This fabric was obtained from STROM Denim-Melita (Malatya, Turkey). The synthesis of the magnetic perovskite-structured $BiFeO_3$ component was accomplished through the utilisation of the modified sol-gel method. The following precursor chemicals were procured for this purpose: bismuth(III) nitrate pentahydrate [$Bi(NO_3)_3 \cdot 5H_2O$, Sigma-Aldrich], iron(III) nitrate nonahydrate [$Fe(NO_3)_3 \cdot 9H_2O$, Sigma-Aldrich], citric acid monohydrate [$C_6H_8O_7 \cdot H_2O$, Sigma-Aldrich], and nitric acid [HNO_3, 65%, Sigma-Aldrich]. Melamine [$C_3H_6N_6$, Sigma-Aldrich], utilized as a precursor in the synthesis of graphitic carbon nitride (g-C_3N_4), was procured. In order to impart superhydrophobic/liquid-repellent properties to the fabric and to anchor functional nanocomposites to the fibers, tetraethyl orthosilicate [TEOS, $Si(OC_2H_5)_4$,

Sigma-Aldrich] and polydimethylsiloxane [PDMS, $[(CH_3)_2SiO]_n$, Sigma-Aldrich] were procured as matrix components. The following solvents were used in the synthesis, coating, and stability tests: analytical-grade ethylene glycol [$C_2H_6O_2$, Sigma-Aldrich], anhydrous ethanol [C_2H_5OH, Sigma-Aldrich], toluene [C_7H_8, Sigma-Aldrich], dichloromethane [DCM, CH_2Cl_2, Sigma-Aldrich], and n-hexane [C_6H_{14}, Sigma-Aldrich].

In order to investigate the effects of acidic and basic environments on the chemical stability of the coating, hydrochloric acid [HCl, Merck] and sodium hydroxide [NaOH, Sigma-Aldrich] were utilized. In the course of photocatalytic performance tests, Rhodamine B [$C_{28}H_{31}ClN_2O_3$, 97%, Sigma-Aldrich] dye was selected as the model organic contaminant. In oil-water separation filtration tests, cationic Methylene Blue dye (Sigma-Aldrich) was utilized to color and monitor the aqueous phase, while the hydrophobic Oil Red O dye (Sigma-Aldrich) was employed to ensure the visibility of dense organic/oil phases (DCM, chloroform, n-hexane). In the scavenger experiments conducted to elucidate the photocatalytic reaction mechanism, 2-propanol (isopropanol, Merck), L-ascorbic acid [$C_6H_8O_6$, Sigma-Aldrich], and EDTA-2Na (Merck) were incorporated into the reaction as scavenger agents. All solutions were prepared using high-purity deionised water.

2.2. Synthesis of $BiFeO_3$@g-C_3N_4 Nanocomposites

The process of synthesising magnetic bismuth ferrite ($BiFeO_3$) nanoparticles was facilitated by a modified sol-gel method. To this end, 0.004 mol of bismuth(III) nitrate pentahydrate ($Bi(NO_3)_3 \cdot 5H_2O$, 1.94 g) and 0.004 mol of iron(III) nitrate nonahydrate ($Fe(NO_3)_3 \cdot 9H_2O$, 1.616 g) were dissolved in 15 mL of ethylene glycol. The pH of the mixture was then adjusted to the 4–5 range using nitric acid (HNO_3) and subjected to ultrasonic treatment for a period of 40 minutes. Subsequently, 0.004 mol of citric acid monohydrate ($C_6H_8O_7 \cdot H_2O$, 0.7684 g) and 5 mL of additional ethylene glycol were added. The solution underwent a 60-minute stirring process at 60°C using a magnetic stirrer, following which it was transferred to a stainless steel autoclave. The solution was then subjected to hydrothermal aging at 100°C for a duration of 16 hours. The resulting product was calcined at a temperature of 500°C for a duration of 3 hours. In order to eliminate impurities, the powder sample was subjected to a washing process consisting of three consecutive centrifugation steps (5000 rpm, 3 minutes) with 0.1 M nitric acid and anhydrous ethanol. Subsequent to this, the sample was dried at a temperature of 80°C.

The material known as graphitic carbon nitride (g-C_3N_4) was synthesised by subjecting melamine to thermal polymerization. Melamine (5 g) was placed into an open porcelain crucible and subsequently annealed in a muffle furnace under an Ar atmosphere. The temperature was elevated to 580°C at a heating rate of 3°C/min, maintained at this temperature under isothermal conditions for 30 minutes, and then permitted to cool spontaneously to room temperature. Following the conclusion of the process, a characteristic light yellow powder sample of g-C_3N_4 was obtained.

The preparation of the $BiFeO_3$@g-C_3N_4 nanocomposite involved dispersing 0.3 g of $BiFeO_3$ and 0.3 g of g-C_3N_4 separately, each in 15 mL of anhydrous ethanol, for a period of 2 hours in an ultrasonic bath. The two suspensions were subsequently combined and homogenised for a further hour in an ultrasonic mixer, after which they were stirred for a total of 24 hours in a magnetic stirrer. The $BiFeO_3$@g-C_3N_4 nanocomposite powder was obtained through a drying process at a temperature of 120°C for a duration of 2 hours.

2.3. Preparation of Superhydrophobic Cotton Fabrics

The coating process was executed through the implementation of a multi-step pad-dry-cure method. In the initial phase of the procedure, the $BiFeO_3$@g-C_3N_4 nanocomposite powder was dispersed in 20 mL of anhydrous ethanol for a duration of 30 minutes in an ultrasonic bath, with the objective of preparing a homogeneous suspension. Cotton fabric samples, previously cleaned with ethanol, were immersed in this suspension and treated in an ultrasonic mixer for 1 hour, followed by drying at 80°C for 10 minutes.

In the subsequent step, a silane matrix was meticulously prepared to facilitate the formation of a low-surface-energy hydrophobic coating on the fabric surface, thereby ensuring the effective anchoring of the nanocomposite particles to the fibers. In order to achieve this objective, a homogeneous sol solution was obtained by mixing PDMS (306 µL) and TEOS (32 µL) in a 10:1 weight ratio in 20 mL of toluene using a magnetic stirrer for 15 minutes. The nanocomposite-coated fabric samples were immersed in the solution, impregnated for a period of 5 minutes, and then dried at a temperature of 80°C for a further 5 minutes. In order to optimise the coating thickness and hydrophobic properties, the immersion-drying cycle was repeated on three occasions. In the final step of the process, the fabric samples were subjected to a cross-linking reaction of the polymeric matrix at 120°C for 1.5

hours. The resulting $BiFeO_3$@g-C_3N_4/TEOS-PDMS-coated cotton fabric samples were stored at room temperature for subsequent characterization and performance testing.

2.4. Characterization techniques

Crystal structure analyzes of the synthesized $BiFeO_3$@g-C_3N_4 nanocomposite structures, intermediate-stage samples, and final modified textile surfaces were conducted using a PANalytical Empyrean diffroctometer with Ni filtered CuKα radition (λ =1.54050 Å; 45 kV and 40 mA) over a 2θ scan range of 10°–80°. In order to elucidate the functional groups and surface chemical bond structures, analyzes were performed in the 4000–400 cm^{-1} range using a Thermo Nicolet 6700 Fourier-transform infrared (FTIR) spectrometer with an ATR accessory. The thermal stability and mass loss profiles of the samples were recorded using thermogravimetric analysis/derivative thermogravimetry/differential scanning calorimetry (TG/DTG/DSC) techniques with a EXSTAR TG/DTA and EXSTAR DSC 7020 apparatus under a dynamic air atmosphere in the temperature range of 25°C to 800°C, and at a constant heating rate of 10°C/min.

The surface morphology and elemental distribution topography of the textile fibers were examined using a Ouanta FEG 450-FEI field-emission scanning electron microscope (FE-SEM) equipped with an energy-dispersive X-ray (EDX) detector. Prior to the imaging process, the sample surfaces were coated with a thin layer of gold to ensure effective conductivity. In order to ascertain the optical bandgap (Eg) values, solid-state UV-Vis diffuse reflectance spectroscopy (DRS) analyzes were conducted in the 200–2500 nm scanning range using a UV–Visible diffused reflectance spectra of samples were measured by Shimadzu UV-3600 Plus UV-Vıs-NIR spectrophotometer equipped with an integrating sphere attachment. In order to ascertain the surface elemental composition and atomic valence states, high-resolution core-level spectra were recorded using a Thermo Scientific K-Alpha X-ray photoelectron spectroscopy (XPS) system equipped with a monochromatic Al Kα (hν = 1486.6 eV) X-ray source. The magnetic behavior and hysteresis (M-H) curves of the samples were measured at room temperature using a Lake Shore Cryotronics vibrating sample magnetometer (VSM) instrument operating within an external magnetic field range of ±20 kOe.

2.5. Wettability and Contact Angle Measurement

The surface wettability of the coated fabrics was determined at room temperature using an ATTENSION-THETALITE contact angle measuring device. Distilled water droplets with a volume of 3 µL were deposited onto the coated fabric surfaces, and the water contact angle (WCA) values were recorded by a video imaging system 15 seconds after contact. The mean of the measurements obtained from five distinct regions of each specimen was employed as the reported value.

In order to evaluate the multi-liquid repellency performance, the instantaneous wettability and static profile behavior of water, milk, cola, coffee, tea, fruit juice and commercial olive oil droplets on the surface were optically recorded. In order to simulate the self-cleaning performance, known as the 'Lotus effect', the samples were mounted on a 15° inclined platform, coated with coffee particles to act as a model particulate contaminant, and then deionised water droplets were continuously applied to the surface using a syringe. The dynamics of the water droplets rolling across the surface and dragging away the coffee particles were visually recorded.

2.6. Durability and Stability Tests

The coating's mechanical wear resistance was assessed through a unidirectional abrasion test, conducted over a 10 cm distance along a straight line on 1000 grit sandpaper. A constant vertical load of 200 g (approximately 1.25 kPa) was applied to the sample surface throughout the test. A WCA measurement was recorded at 10-cycle intervals, with a total of 50 cycles (corresponding to a 5 m total abrasion path) being completed.

The coating's structural resistance to household washing processes was evaluated in accordance with AATCC 61 No. 1A by subjecting it to a mechanical washing cycle at 40°C in a 0.37% standard detergent-water solution (200 mL), with 10 stainless steel balls, at a rotation speed of 40 rpm for 45 minutes.

The chemical stability of the coating was assessed through a series of immersions in diverse solution environments, encompassing acidic (pH 2, HCl), basic (pH 12, NaOH), and saline (3.5% NaCl) solutions. These immersions were maintained for a duration of 24 hours. The resistance of the samples to organic solvents was evaluated through a process of immersion in chloroform, dichloromethane (DCM), and toluene for a period of 24 hours. Subsequent to the completion of all tests, the samples were rinsed with deionised water and dried. Thereafter, their WCA values were remeasured in order to confirm the preservation of their superhydrophobic properties.

2.7. Oil-Water Separation Performance

The oil-water separation performance of the superhydrophobic/superoleophilic-coated fabrics was evaluated using a gravity-driven filtration setup. Dichloromethane (DCM, ρ = 1.325 g/mL) was utilized as the heavy oil phase, while n-hexane (ρ = 0.659 g/mL) was employed as the light oil phase. In order to facilitate visual monitoring of phase separation, the oil phases were dyed with a trace amount of Oil Red O, while the pure water phase was dyed with a trace amount of Methylene Blue. The modified fabric samples were fixed at the neck of a funnel apparatus, and oil-water mixtures (50:50, v/v) were passed through the fabric barrier under the effect of gravity.

The oil-water separation efficiency (η, %) was calculated using Eq. (1):

$$\eta(\%) = \left(\frac{m_1}{m_0}\right) \times 100 \quad (1)$$

where m_0 and m_1 represent the mass of oil collected before and after the filtration process (g), respectively.

The filtration flux (J, $L \cdot m^{-2} \cdot h^{-1}$) was calculated using Eq. (2):

$$J = \frac{V}{A \cdot \Delta t} \quad (2)$$

where V denotes the volume of filtered oil (L), A denotes the effective surface area of the fabric (m^2), and Δt denotes the filtration duration (h). The stability and reusability of the system were tested over 10 consecutive cycles using the same fabric sample.

2.8. Photocatalytic Activity and Radical Scavenger Experiments

The photocatalytic performance of the coated fabrics was evaluated based on the photodegradation of Rhodamine B (RhB) dye under UVA and visible light irradiation. The experiments were conducted at ambient temperature in a controlled photoreactor (Luzchem LZC-4X). Fabric samples measuring 4 × 4 cm^2 were immersed in 100 mL of an aqueous solution of RhB (1.25 mg/L). Prior to the commencement of the light exposure, the system was subjected to a 60-minute period of darkness on a magnetic stirrer, with the objective of establishing adsorption-desorption equilibrium. Following the determination of the initial concentration (C_0), the light source was activated, and 1 mL of sample was withdrawn at predetermined time intervals to measure the instantaneous concentration (C_t) at a wavelength of 554 nm—the characteristic absorption peak of RhB—using a UV-Vis spectrophotometer. Subsequent to the measurement process, the sample was returned to the reaction vessel. The photocatalytic degradation efficiency (%) was calculated using Eq. (3):

$$Photocatalytic\ degradation\ efficiency\ (\%) = \left(\frac{C_0 - C_t}{C_0}\right) \times 100 \quad (3)$$

In the scavenger experiments conducted to identify active and reactive radical species (•OH, $\bullet O_2^-$, h^+), target scavenger agents were added at a concentration of 1 mM prior to exposing the photocatalytic system to light. 2-Propanol (isopropanol) was used to mask •OH radicals, L-ascorbic acid to capture $\bullet O_2^-$ radicals, and EDTA-2Na to inhibit h^+ holes. Comparative kinetic analyzes were performed against control experiments lacking scavengers. In order to assess the long-term stability of the coating, five consecutive photocatalytic cycles were conducted on a single fabric sample, and the repeatability of the results was documented.

3. RESULTS AND DISCUSSION

3.1. Structural and Morphological Characterization

3.1.1. XRD Analysis

X-ray diffraction (XRD) analysis was employed to verify the crystal structures, phase purity, and crystallinity of the synthesized nanostructures, as well as to assess successful coating of these nanostructures onto the cotton fabric (Fig. 1a-d). The XRD pattern of untreated cotton exhibited the distinctive diffraction peaks at 15.03°, 16.98°, 22.88°, and 34.87° (2θ), with d-spacings of 5.89, 5.31, 3.88, and 2.57 Å, corresponding to the crystallographic planes (1-10), (110), (200), and (004) of cellulose Iβ, respectively, in good agreement with the characteristic

crystalline structure previously reported for cotton fibers (Fig. 1a) (Kashem et al. 2026; Pawar et al. 2025; Özdemir et al. 2022). The simultaneous occurrence of broad and sharp diffraction peaks reflects the presence of both amorphous and crystalline phases within the cotton fibers, confirming the intrinsic semi-crystalline structure inherent to native cellulose-based textile materials.

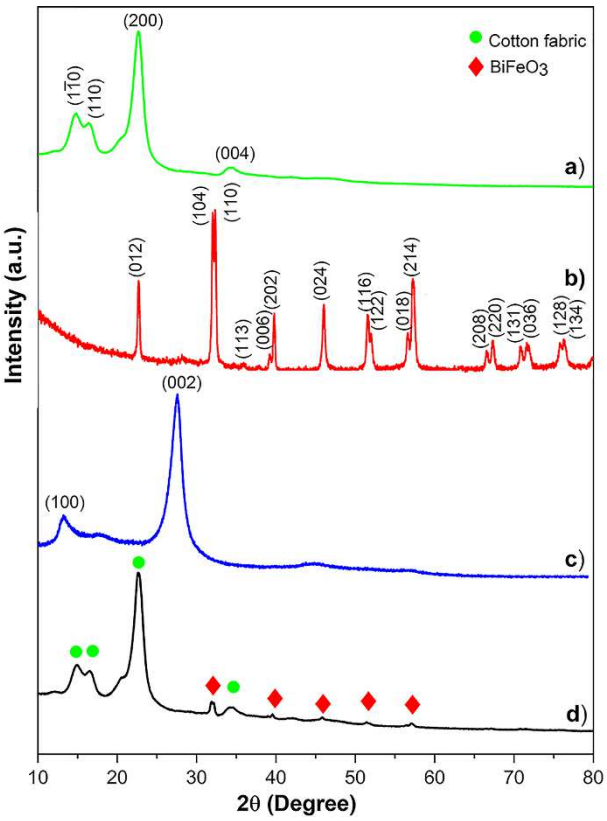


Figure 1. XRD patterns of (a) untreated cotton fabric, (b) BiFeO3 nanoparticles, (c) g-C_3N_4, and (d) $BiFeO_3$@g-C_3N_4/TEOS-PDMS-coated cotton

The XRD pattern of the synthesized BiFeO3 nanoparticles exhibited characteristic diffraction peaks at 22.41°, 31.75°, 32.07°, 37.65°, 39.47°, 39.58°, 45.75°, 51.30°, 51.74°, 56.35°, 57.11°, and 57.18° (2θ), corresponding to d-spacings of 3.96, 2.82, 2.79, 2.38, 2.29, 2.28, 1.98, 1.78, 1.77, 1.63, 1.61, and 1.60 Å, respectively (Fig. 1b). These reflections were indexed to the (012), (104), (110), (113), (006), (202), (024), (116), (122), (018), (214), and (300) crystallographic planes, confirming the formation of a rhombohedral distorted perovskite BiFeO3 phase with an R3c space group, in excellent agreement with the standard JCPDS Card No. 71-2494 (Caglar et al. 2021a, 2021b). The sharp, well-defined, and intense diffraction peaks, together with the absence of detectable reflections from secondary impurity phases, confirm the successful synthesis of highly crystalline and phase-pure BiFeO3 nanoparticles.

The XRD pattern of g-C3N4 demonstrated two characteristic peaks at 12.95° and 27.42° (2θ), with d-spacings of 6.90 and 3.25 Å, corresponding to the (100) and (002) crystal planes, respectively (Fig. 1c) (JCPDS Card No. 87-1526; Hao et al. 2018). The first peak is related to the in-planar structural packing motif of tri-s-triazine units maintained by hydrogen bonds, whereas the second peak is attributed to the interlayer stacking of aromatic systems governed by van der Waals interactions (Lan et al. 2017; Yang et al. 2022; Shao et al. 2016).

Notably, the XRD pattern of the $BiFeO_3$@g-C_3N_4/TEOS-PDMS-coated cotton fabric exhibited the characteristic diffraction peaks of both cellulose and the BiFeO3 nanoparticles, confirming the successful incorporation of $BiFeO_3$@g-C_3N_4 onto the cotton fabric (Fig. 1d). However, no distinct diffraction peaks corresponding to the g-C_3N_4 phase were observed, suggesting that the partial exfoliation and uniform assembly of g-C_3N_4 nanosheets on the cotton fibers effectively inhibited their restacking, thereby reducing the detectable crystallinity of g-C_3N_4 and promoting its homogeneous dispersion within the composite; any remaining reflections were likely masked by the dominant diffraction peaks of cellulose, without causing any appreciable change in the crystallinity of the cotton fibers (Glažar et al. 2026; Majdoub et al. 2025; Fan et al. 2018). Furthermore, the diffraction profile of the coated

cotton fabric unequivocally demonstrates that the $BiFeO_3$ phase remained structurally intact throughout the coating process, without undergoing detectable decomposition or phase transformation. Overall, these findings confirm the successful coating of the related components onto the cotton fabric, leading to the formation of a stable and functional composite structure.

3.1.2. FTIR Analysis

The FTIR spectrum of pristine cotton fabric (Fig. 2a) exhibited the characteristic absorption bands of cellulose, including the broad O-H stretching of hydrogen-bonded hydroxyl groups at 3326 cm^{-1}, the aliphatic C-H stretching vibration at 2895 cm^{-1}, and the adsorbed water bending vibration at 1627 cm^{-1} (El-Shishtawy et al. 2011; Diao et al. 2026). The absorption bands at 1428 and 1313 cm^{-1} were assigned to CH2 symmetric bending and C-H wagging vibrations, respectively, while the intense peak centered at 1019 cm^{-1} corresponded to the characteristic C-O stretching together with C-C stretching and ring skeletal vibrations of the cellulose backbone. Furthermore, the characteristic bands observed at 893 and 661 cm^{-1} were attributed to the β-glycosidic C-O-C linkage and out-of-plane C-O-H bending vibrations, confirming the characteristic molecular structure of native cellulose (El-Shishtawy et al. 2011; Diao et al. 2026).

The FTIR spectrum of $BiFeO_3$ nanoparticles (Fig. 2b) revealed two characteristic bands at 530 and 425 cm^{-1}, corresponding to the Fe-O stretching and bending vibrations of FeO6 octahedra within the perovskite crystal lattice, respectively, confirming the successful formation of crystalline BiFeO3 (Caglar et al. 2021a, 2021b).

Likewise, the FTIR spectrum of g-C_3N_4 (Fig. 2c) exhibited a broad and relatively weak absorption band in the range of 3000-3400 cm^{-1}, which corresponds to the stretching vibrations of terminal N-H groups in the aromatic ring (Yan and Yang 2011; Benisti et al. 2021). The band at 1628 cm^{-1} is ascribed to the C=N stretching vibration, whereas the peaks at 1543, 1397, 1316, and 1230 cm^{-1} are attributed to aromatic C-N stretching vibrations. In addition, the characteristic absorption band observed at 805 cm^{-1} is assigned to the breathing mode of the tri-s-triazine units or the out-of-plane conjoint wagging vibrations of C and N atoms in the heptazine framework. This band represents the characteristic structural fingerprint of graphitic carbon nitride, demonstrating the successful synthesis of g-C_3N_4 (Yan and Yang 2011; Benisti et al. 2021; Bian et al. 2016).

Prior to introducing the TEOS/PDMS binder system, the intermediate $BiFeO_3$@g-C_3N_4-coated cotton fabric (Fig. 2d) clearly retained the characteristic vibrational bands of cellulose, $BiFeO_3$, and g-C_3N_4 simultaneously. In particular, the Fe-O vibrational bands of BiFeO3 together with the characteristic heptazine-ring vibration of g-C_3N_4 remained clearly distinguishable, demonstrating that both inorganic and carbon nitride components were successfully deposited onto the cellulose fibers while preserving their intrinsic chemical structures. The coexistence of these characteristic absorption bands provides direct evidence for the successful coating of the $BiFeO_3$@g-C_3N_4 nanocomposite onto the cotton fiber.

Following subsequent treatment with the TEOS/PDMS system (Fig. 2e), the FTIR spectrum underwent significant spectral changes, revealing the formation of an inorganic-organic hybrid siloxane network on the cotton surface. A newly emerged absorption band at 2962 cm^{-1} was assigned to the symmetric C-H stretching of Si-CH_3 groups originating from PDMS, while the characteristic bands at 1258 and 789 cm^{-1} corresponded to the symmetric deformation of Si-CH_3 and the Si-C stretching vibration, respectively, confirming the successful incorporation of PDMS into the cotton fiber (Wu et al. 2021; Zhao K et al. 2026). The most significant spectral evolution occurred within the 1000-1100 cm^{-1} region, where the characteristic C-O stretching vibration of cellulose overlapped with the asymmetric stretching vibrations of Si-O-Si bonds, resulting in a considerably sharper and more intense absorption band at 1023 cm^{-1}. Such spectral changes strongly indicate that the hydrolysis and condensation of TEOS generated an extensively cross-linked siloxane framework, through which the hydroxyl-rich cellulose surface and the BiFeO3@g-C3N4 nanocomposite were chemically interconnected via covalent siloxane linkages. Meanwhile, the reduced intensity and partial masking of the characteristic Fe-O and g-C_3N_4 bands are attributed to the dense encapsulation of the nanocomposite particles within the PDMS/TEOS hybrid matrix rather than to structural degradation. Collectively, these spectral features unequivocally demonstrate the successful fabrication of a covalently integrated $BiFeO_3$@g-C_3N_4/TEOS-PDMS hybrid coating, in which the silicone-rich outer layer enriched with low-surface-energy Si-CH_3 groups is responsible for the establishment of the superhydrophobic surface (Wu et al. 2021; Lu et al. 2026).

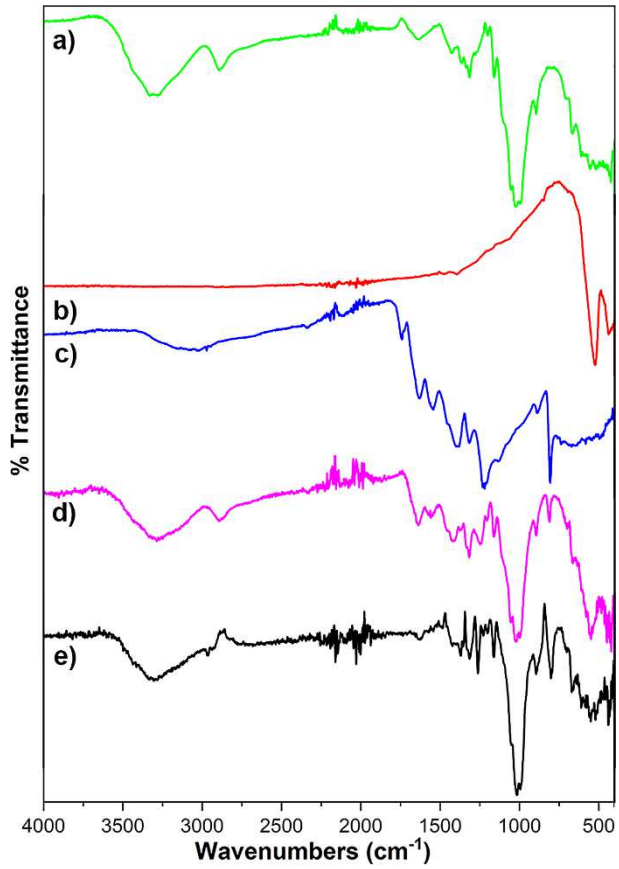


Figure 2. FTIR spectra of (a) untreated cotton fabric, (b) $BiFeO_3$ nanoparticles, (c) g-C_3N_4, (d) $BiFeO_3$@g-C_3N_4-coated cotton fabric, and (e) $BiFeO_3$@g-C_3N_4/TEOS-PDMS-coated cotton fabric

3.1.3. SEM-EDX Analysis

Figure 3(a-c) shows the SEM images of the untreated cotton fabric at different magnifications. At low magnification (a, 500 µm), the warp-weft weave structure is clearly observed, and the regular weaving geometry of the yarn bundles is preserved (Wei et al. 2020). At medium magnification (b, 20 µm), the characteristic twisted-ribbon morphology of individual cotton fibers and the natural waxy cuticle layer are visible (Wakelyn et al. 2006). At high magnification (c, 5 µm), the fiber surface is confirmed to exhibit a relatively flat, slightly longitudinally striated, and non-porous topography; this appearance is consistent with the flat and smooth surface morphology reported in the literature for untreated cellulosic substrates (Türe 2025). These morphological observations are supported by the EDAX results: only C (47.51%) and O (52.49%) elements were detected in the fabric, and this ratio is quite close to the theoretical weight-based composition of pure cellulose (C is approximately 47.4%, O is approximately 52.6%) (Badawi et al. 2023; see Online Resource 1). The absence of any foreign element (Si, Bi, Fe, etc.) confirms the pre-treatment purity of the fabric and its homogeneous cellulosic structure, consistent with its flat/smooth surface morphology.

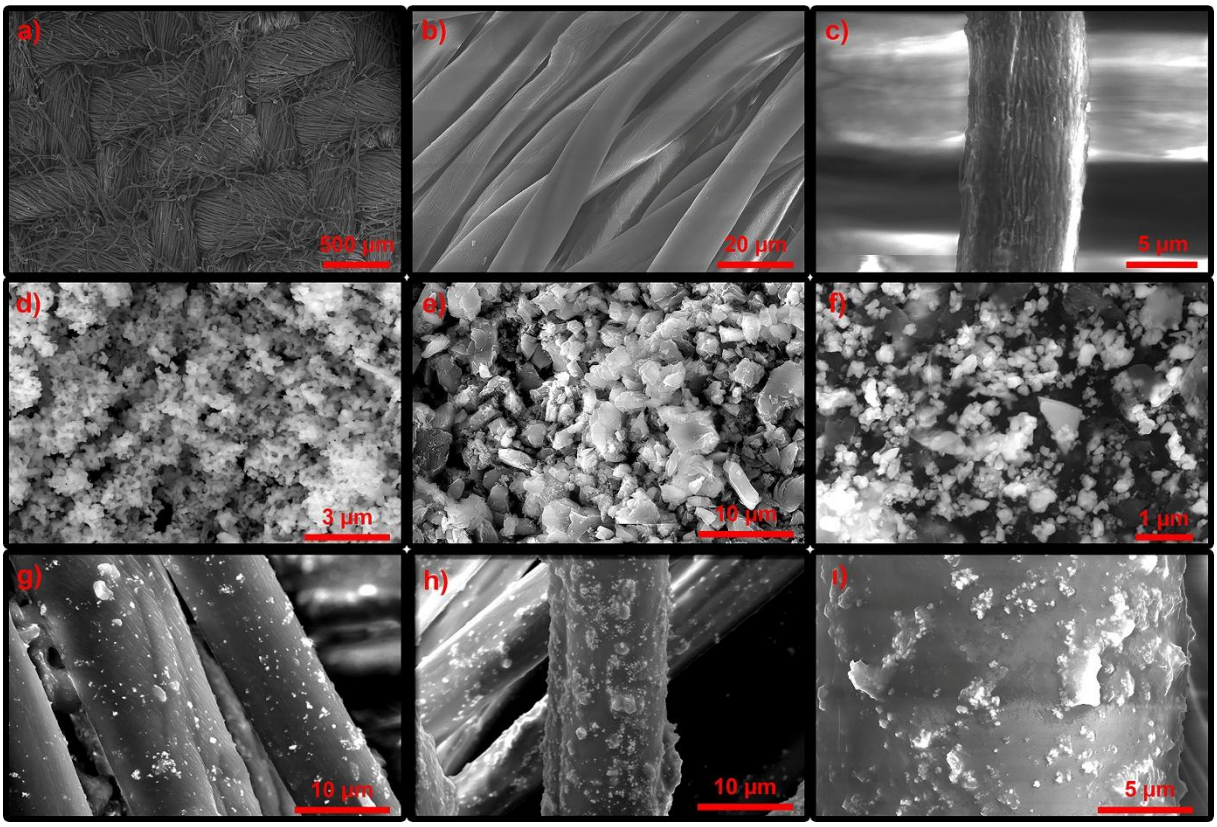


Figure 3. SEM images: (a-c) untreated cotton fabric (at 500 µm, 20 µm, and 5 µm magnifications, respectively), (d) pristine $BiFeO_3$, (e) pristine g-C_3N_4, (f) $BiFeO_3$@g-C_3N_4 composite powder, (g-i) $BiFeO_3$@g-C_3N_4/TEOS-PDMS-coated cotton fabric (at 10 µm, 10 µm, and 5 µm magnifications, respectively)

Figure 3(d) presents the SEM image of pristine $BiFeO_3$ powder. Nanometer-sized particles are observed to be densely agglomerated, exhibiting a homogeneous, granular morphology with particles of similar size; this appearance is consistent with the typical morphology reported in the literature for perovskite-structured $BiFeO_3$ synthesized via sol-gel/hydrothermal methods (Caglar et al. 2021b; Deeksha et al. 2023; Xu et al. 2024). In parallel, EDAX analysis detected Bi (63.3%), Fe (18.85%), and O (17.86%) elements, values close to the stoichiometric BiFeO3 composition (Bi:Fe:O is approximately 67:18:15, by weight). The absence of any signal corresponding to another cation or impurity phase (e.g., Bi_2O_3, Fe_2O_3) is consistent with the single-type granular morphology observed by SEM and, together with the XRD data, confirms the formation of single-phase, pure $BiFeO_3$ (see Online Resource 2).

Figure 3(e) shows the characteristic two-dimensional lamellar/flake-like structure of pristine g-C_3N_4. This morphology, consisting of layered platelets with irregular edges, is a typical feature of g-C3N4 obtained via thermal polycondensation (Saravanakumar and Park 2021; Xu et al. 2024). In the EDAX analysis, C (33.4%) and N (66.6%) elements were predominantly observed, and the experimental C:N atomic ratio was found to be approximately 0.58 (compared with approximately 0.75 for theoretical C3N4); this decrease can be explained by the partial nitrogen enrichment resulting from incomplete condensation of the tri-s-triazine rings. Indeed, it has been reported in the literature that, in incompletely condensed g-C_3N_4 structures, the C/N ratio deviates from the ideal value (approximately 0.75), and this deviation originates from residual surface amino (-NH_2/-NH) groups, which contribute to surface reactivity (Pei et al. 2023; see Online Resource 3).

Figure 3(f) is the SEM image of the $BiFeO_3$@g-C_3N_4 composite powder. Relatively homogeneously distributed, small $BiFeO_3$ nanoparticles are clearly observed to decorate the lamellar skeleton of g-C_3N_4. This morphological appearance suggests that the two phases are not merely physically coexisting, but rather form a closely contacted interface (Xu et al. 2024). The EDAX results directly support this observation: the simultaneous detection of C (29.63%), N (43.42%), O (10.95%), as well as Bi (9.3%) and Fe (6.7%), is direct evidence that $BiFeO_3$ nanoparticles were successfully loaded onto the g-C_3N_4 matrix. The overlap between the Bi and Fe signals and the particle-plate morphology observed by SEM indicates that the two phases form a molecularly interacting composite rather than a macroscopic mixture (see Online Resource 4).

Figure 3(g-i) presents the SEM images of the $BiFeO_3$@g-C_3N_4/TEOS-PDMS-coated cotton fabric. At low magnification (g), a rough and granular coating layer is observed to have formed on the fiber surface, in contrast to the untreated fabric (compared with b), with particle clusters distributed along the fiber. At medium magnification (h), the coating on an individual fiber appears relatively homogeneous and continuous, with sub-micron-sized particles firmly adhering to the fiber surface. At high magnification (i, 5 μm), the hierarchical micro/nano-roughness formed by $BiFeO_3$@g-C_3N_4 particles embedded within the TEOS-PDMS matrix is clearly observed; this dual-scale roughness, combined with the low-surface-energy PDMS component, provides the morphological prerequisite required for the Cassie-Baxter state expected on superhydrophobic surfaces. Indeed, a similar increase in surface roughness has been shown to markedly raise the water contact angle on cellulosic substrates (Türe 2025). These morphological findings are consistent with the EDAX analysis: in addition to C (31.65%), N (21.03%), and O (44.3%), Si (1.31%), Bi (0.85%), and Fe (0.86%) elements were also detected in the coated fabric. The emergence of the Si signal is direct evidence that the continuous, rough coating layer observed by SEM is the TEOS/PDMS-derived silane network; the presence of N and Bi/Fe signals (albeit at low intensity) confirms that the particle clusters observed by SEM belong to the $BiFeO_3$@g-C_3N_4 photocatalyst. The relatively low weight percentages of Bi and Fe indicate that these elements are present as a sub-phase partially covered by the organosilicon matrix on the outer surface, which can be interpreted as the coating exhibiting a layered structure between the PDMS/TEOS-dominant outer surface and the underlying photocatalyst-cellulose core (Abu Bakar et al. 2024; Ghosh et al. 2025; see Online Resource 5). The elemental compositions of all investigated samples, as determined by EDAX, are summarized in Table 1.

Table 1. Elemental composition of the samples as determined by EDAX (wt%)

Sample	**C**	**N**	**O**	**Si**	**Fe**	**Bi**
Untreated cotton	47.51	–	52.49	–	–	–
Pure $BiFeO_3$	–	–	17.86	–	18.85	63.3
Pure g-C_3N_4	33.4	66.6	–	–	–	–
$BiFeO_3$@g-C_3N_4	29.63	43.42	10.95	–	6.7	9.3
$BiFeO_3$@g-C_3N_4/TEOS-PDMS@fabric	31.65	21.03	44.3	1.31	0.86	0.85

3.1.4. XPS Analysis

To further verify the successful fabrication of the $BiFeO_3$@g-C_3N_4/TEOS-PDMS-coated cotton fabric, as well as to investigate its surface elemental composition and chemical states, X-ray photoelectron spectroscopy (XPS) analysis was performed. The survey XPS spectrum (Fig. 4a) clearly reveals the presence of C, O, Si, N, Bi, and Fe elements without detectable impurity peaks, confirming the successful deposition of the TEOS-PDMS coating together with the $BiFeO_3$@g-C_3N_4 nanostructure onto the cotton substrate. The C 1s, O 1s, and Si 2p signals exhibit considerably higher intensities than the remaining elemental peaks. This behavior is primarily attributed to the cellulose-rich nature of the cotton substrate, which contributes strong C and O signals, together with the continuous TEOS-PDMS siloxane network that uniformly coats the fabric surface and provides an additional Si- and O-rich overlayer. In contrast, the Fe 2p and N 1s peaks exhibit relatively low intensities in the survey spectrum, which can be attributed to the surface-sensitive nature of XPS with an effective information depth of approximately 5-10 nm, the partial encapsulation of the BiFeO3@g-C3N4 nanostructure within the TEOS-PDMS siloxane layer, and the relatively low surface atomic concentrations of Fe and N. Similar observations have been reported for PDMS-coated hybrid cotton fabric systems embedded with nanospecies (Wu et al. 2021; Han et al. 2026; Shi et al. 2024).

The high-resolution C 1s spectrum of the $BiFeO_3$@g-C_3N_4/TEOS-PDMS-coated cotton fabric (Fig. 4b) was deconvoluted into four characteristic peaks centered at 284.23, 285.45, 287.50, and 289.75 eV. The peak at 284.23 eV is assigned to C-C/C-H bonds originating from the cellulose backbone of the cotton substrate and the methyl groups of PDMS. The peak at 285.45 eV is attributed to C-Si bonds from the PDMS coating together with C-NH species associated with the g-C_3N_4 framework. The peak centered at 287.50 eV corresponds to C-O-C groups in cellulose and N-C=N (or C-N-C) species in the heptazine units of g-C3N4, whereas the weak peak at 289.75 eV is assigned to O-C=O species, which are attributed to slight oxidation of the cellulose surface during the coating process (Shi et al. 2024; Zhao K et al. 2026).

The high-resolution O 1s spectrum of the $BiFeO_3$@g-C_3N_4/TEOS-PDMS-coated cotton fabric (Fig. 4c) was deconvoluted into five components centered at 531.93, 533.32, 534.37, 535.15, and 536.39 eV. The dominant peak at 531.93 eV is assigned to lattice oxygen (Bi-O and Fe-O bonds) in the perovskite $BiFeO_3$ structure, confirming the presence of the $BiFeO_3$ nanoparticles on the coated fabric surface. The component at 533.32 eV is attributed to Si-O-Si bonds originating from the highly cross-linked siloxane network formed through the hydrolysis and condensation of TEOS and PDMS. The peak centered at 534.37 eV is assigned to oxygen in C-O/C-O-C groups of the cellulose substrate together with residual Si-OH species in the siloxane network. The weak high-binding-energy components located at 535.15 and 536.39 eV are attributed to surface oxygen species associated with terminal silanol groups, hydrogen-bonded oxygen environments, and other high-energy oxygen states within the hybrid siloxane network (Lu et al. 2026). The relatively low intensities of these two components indicate that they represent minor surface oxygen environments rather than the predominant oxygen species, which is consistent with the formation of a densely cross-linked TEOS-PDMS coating over the $BiFeO_3$@g-C_3N_4-modified cotton substrate.

The high-resolution Si 2p spectrum (Fig. 4d) was deconvoluted into four components centered at 101.85, 103.07, 104.90, and 105.97 eV. The component at 101.85 eV is characteristic of Si-C bonds arising from the methyl groups in the PDMS backbone (Kuroki et al. 1998; Golubchikov et al. 2025). The dominant peak at 103.07 eV corresponds to the Si-O-Si siloxane linkages, confirming the formation of a cross-linked network derived from TEOS and PDMS co-condensation (Al-Shaeli et al. 2026; Park et al. 2022). The higher binding energy peak at 104.90 eV is assigned to Si-O-C interfacial covalent bonding formed between the silanol species and the cellulosic hydroxyl groups of the cotton fiber, together with highly condensed [SiO_4] silicate units. Finally, the component located at 105.97 eV is attributed to interfacial interactions between the organosilicon matrix and the embedded perovskite nanoparticles, alongside slight differential surface charging intrinsically associated with the insulating nature of the thick silane/polymeric coating (Park et al. 2022). These findings unambiguously verify the chemical coupling of the hybrid coating to both the inorganic photocatalyst and the organic textile substrate.

The high-resolution N 1s spectrum (Fig. 4e) was deconvoluted into four components centered at 394.88, 398.70, 401.70, and 406.62 eV. The dominant peak at 398.70 eV is assigned to the sp2-hybridized C-N=C species in the heptazine units of graphitic carbon nitride (g-C_3N_4) (Li et al. 2025). The component centered at 401.70 eV is attributed to graphitic nitrogen [N-$(C)_3$], corresponding to tertiary nitrogen atoms incorporated within the conjugated g-C_3N_4 framework (Ma et al. 2024). The low-binding-energy feature observed at 394.88 eV is attributed to nitrogen species involved in strong interfacial electronic interactions with the BiFeO3 phase, suggesting charge redistribution at the $BiFeO_3$/g-C_3N_4 heterointerface. The weak high-binding-energy component located at 406.62 eV is assigned to pi-pi shake-up satellite features and/or oxidized nitrogen species generated during surface modification (Guo et al. 2024; Li et al. 2025). Collectively, the N 1s spectrum confirms that the graphitic carbon nitride framework remains chemically stable after incorporation into the TEOS-PDMS hybrid coating while exhibiting electronic interaction with the BiFeO3 phase.

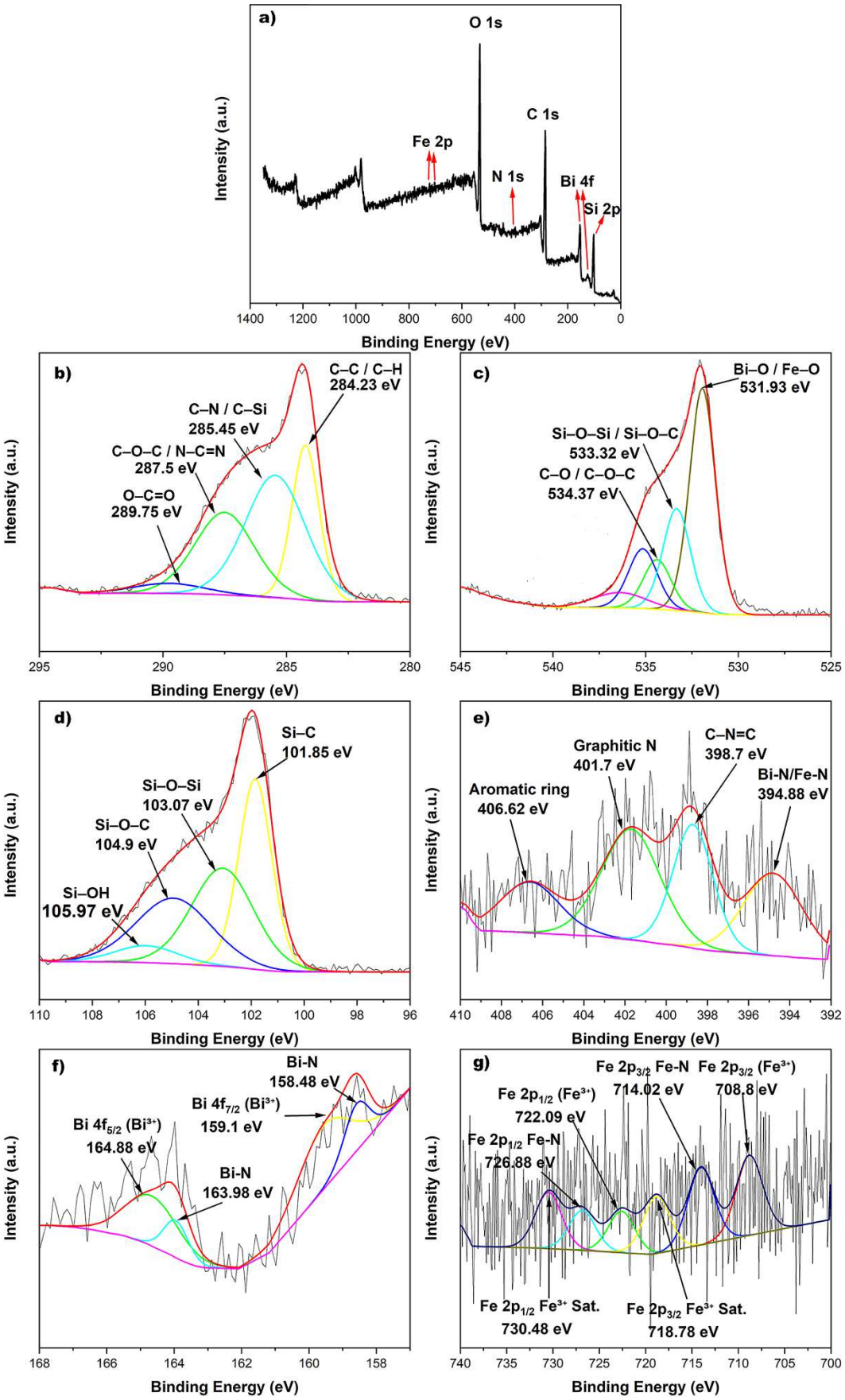


Figure 4. XPS spectra of the $BiFeO_3$@g-C_3N_4/TEOS-PDMS-coated cotton fabric: (a) survey spectrum, and high-resolution spectra of (b) C 1s, (c) O 1s, (d) Si 2p, (e) N 1s, (f) Bi 4f, and (g) Fe 2p

The high-resolution Bi 4f spectrum (Fig. 4f) exhibits two characteristic spin-orbit doublets. The peaks located at 159.10 and 164.88 eV are assigned to the Bi 4f7/2 and Bi 4f5/2 states of Bi3+ in the perovskite $BiFeO_3$ lattice, confirming that bismuth remains in its trivalent oxidation state after the coating process (Gomez-Iriarte et al. 2022). In addition, the weak low-binding-energy components observed at 158.48 and 163.98 eV are attributed to Bi species experiencing modified electronic environments owing to interfacial interaction with the nitrogen-rich g-C_3N_4 framework (Guo et al. 2024). The coexistence of these components suggests electronic coupling between $BiFeO_3$ and g-C_3N_4 without altering the crystal structure of the BiFeO3 phase.

The high-resolution Fe 2p spectrum (Fig. 4g) displays two characteristic spin-orbit doublets corresponding to Fe 2p3/2 and Fe 2p1/2. The principal peaks centered at 708.80 and 722.09 eV are assigned to Fe^{3+} species in the $BiFeO_3$ lattice (Gomez-Iriarte et al. 2022; Upar et al. 2023). The additional components located at 714.02 and 726.88 eV are attributed to multiplet splitting and changes in the electronic environment resulting from interfacial interaction between $BiFeO_3$ and the g-C_3N_4 matrix (Guo et al. 2024; Upar et al. 2023). Furthermore, the satellite peaks observed at approximately 718.78 and 730.48 eV are characteristic of Fe^{3+} species and further confirm the preservation of the perovskite $BiFeO_3$ structure (Grosvenor et al. 2004; Li et al. 2025). The Fe 2p spectrum therefore indicates that the oxidation state of iron is maintained after deposition and subsequent encapsulation within the TEOS-PDMS siloxane coating while evidencing electronic coupling at the $BiFeO_3$/g-C_3N_4 heterointerface.

3.1.5. TGA/DTG/DSC Analysis

As shown in the TG curves (Fig. 5a), all samples exhibited only a slight mass loss below approximately 100 °C, which can be attributed to the removal of trace physically retained volatile species. Notably, the Cotton/$BiFeO_3$@g-C_3N_4/TEOS-PDMS sample exhibited an almost negligible mass loss in this temperature region, indirectly confirming the highly hydrophobic nature of the superhydrophobic coating and its remarkably low affinity toward moisture adsorption. Subsequently, the principal degradation stage occurred within the temperature range of approximately 300-390 °C, corresponding to the typical pyrolytic decomposition of cellulose, including depolymerization of the cellulose backbone, cleavage of glycosidic linkages, dehydration reactions, and the evolution of volatile degradation products (Wu et al. 2021; Lu et al. 2026). This thermal degradation behavior is in good agreement with the characteristic pyrolysis mechanism reported for cellulose-based textile materials (Zhao K et al. 2026; Wu et al. 2021; Lu et al. 2026).

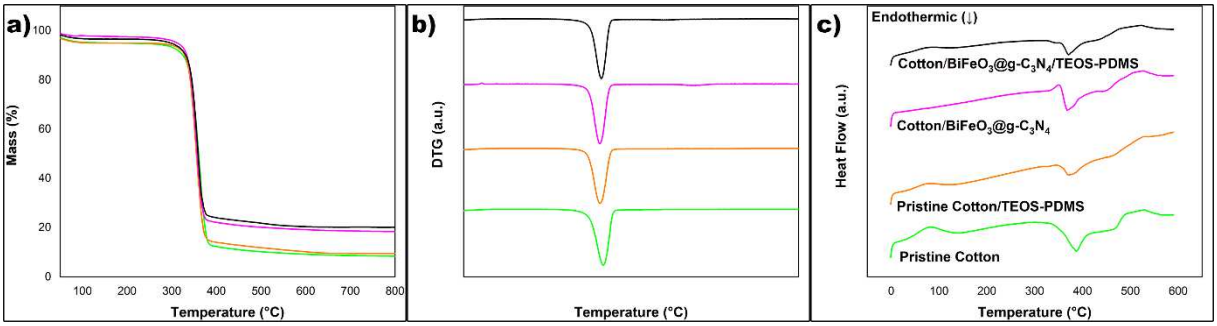


Figure 5. (a) TG, (b) DTG, and (c) DSC curves of pristine cotton, Cotton/TEOS-PDMS, Cotton/$BiFeO_3$@g-C_3N_4, and Cotton/$BiFeO_3$@g-C_3N_4/TEOS-PDMS

Pristine cotton reached its maximum degradation rate at approximately 362 °C, as confirmed by the DTG curves (Fig. 5b), followed by a rapid weight loss associated with the extensive decomposition of cellulose chains. Consequently, only 8.4% residual char remained at 800 °C, indicating the inherently low carbonization efficiency of untreated cellulose due to its extensive conversion into volatile decomposition products during pyrolysis (Han et al. 2026; Feng et al. 2026).

Modification of the cotton fabric with TEOS-PDMS caused only a slight change in the maximum degradation temperature, whereas the residual mass at elevated temperatures increased noticeably. The residual char yield reached approximately 9.6% at 800 °C, suggesting that the thermally stable Si-O-Si backbone of PDMS together with the silica-like three-dimensional network generated through TEOS hydrolysis formed a protective ceramic-like barrier during thermal decomposition (Zhao Q et al. 2026). This cross-linked siloxane network effectively restricted heat transfer and suppressed the diffusion of volatile degradation products, thereby promoting carbonization and enhancing the thermal resistance of the cotton substrate (Zhao Q et al. 2026).

A substantially greater improvement in thermal stability was achieved for the Cotton/$BiFeO_3$@g-C_3N_4 composite. Although the maximum degradation temperature remained close to 356 °C, the overall weight loss at elevated temperatures was significantly reduced, resulting in a residual char yield of approximately 18.4% at 800 °C. Compared with pristine cotton, this more than twofold increase in residual mass demonstrates the remarkable contribution of the $BiFeO_3$ perovskite nanoparticles and layered g-C_3N_4 nanosheets to thermal stabilization. These inorganic phases act as efficient thermal shielding layers, retarding heat transfer and suppressing the release of volatile pyrolysis products while simultaneously facilitating char formation. Consequently, the formation of a dense and thermally stable protective carbonaceous layer effectively delays the progression of thermal degradation and significantly improves the high-temperature stability of the coated fabric (Zhao K et al. 2026).

Among all investigated samples, the Cotton/$BiFeO_3$@g-C_3N_4/TEOS-PDMS hybrid coating exhibited the highest thermal stability. The maximum degradation temperature increased to approximately 360 °C, while the residual char yield further increased to approximately 20.2% at 800 °C, representing the highest thermal resistance within the series. This superior performance arises not only from the intrinsic thermal stability of the $BiFeO_3$/g-C_3N_4 nanocomposite but also from the cross-linked siloxane network formed by TEOS-PDMS, which firmly anchors the nanocomposite onto the cotton fibers. The resulting hybrid architecture creates an integrated, multilayered protective barrier that simultaneously suppresses heat transfer and inhibits the diffusion of volatile degradation products during pyrolysis, thereby substantially promoting carbonization (Zhao Q et al. 2026; Zhao K et al. 2026). The synergistic interaction between the inorganic nanocomposite and the siloxane matrix is therefore responsible for the outstanding thermal stability of the hybrid-coated fabric.

The DSC results (Fig. 5c) are also consistent with the TG and DTG analyzes. Pristine cotton displayed a pronounced endothermic event at approximately 360-370 °C, whereas the coated fabrics exhibited weaker and broader endothermic peaks, suggesting a more controlled thermal degradation process with reduced instantaneous energy consumption. Furthermore, the heat-flow variations observed between 450 and 550 °C imply the continued structural evolution of the coating system, which may be associated with the rearrangement of the siloxane network and the formation of silica-derived ceramic structures from PDMS, together with the excellent thermal stability of the $BiFeO_3$/g-C_3N_4 nanocomposite (Zhao Q et al. 2026; Zhao K et al. 2026). This interpretation is fully consistent with the higher residual char yields observed in the TG curves and further confirms that the hybrid coating effectively preserves its structural integrity at elevated temperatures.

3.1.6. VSM Analysis

Vibrating Sample Magnetometer (VSM) analysis was performed at room temperature (298 K) in order to determine the magnetic characteristics of the developed $BiFeO_3$@g-C_3N_4/TEOS-PDMS hybrid-coated textile surface, its response dynamics under an applied magnetic field, and its practical recoverability potential from photocatalytic reaction media. The M-H hysteresis loop, presenting the variation of magnetization (M) as a function of the applied magnetic field (H) for the hybrid fabric sample with a mass of 6.90 mg, is shown in Figure 6.

The narrow and symmetric hysteresis loop observed in Figure 6 reveals that the system exhibits soft ferromagnetic behavior, attributed to the presence of the inorganic perovskite BiFeO3 phase on the modified fabric surface (Shah et al. 2014; Čebela et al. 2025). Upon examination of the curve behavior in the high-field region, the maximum mass magnetization measured under a 20 kOe external field was found to be 27.12 emu/g, while the extrapolated saturation magnetization (Ms) was determined to be 30.62 emu/g. Considering the dominant contribution of the ultrathin polymeric silane matrix (TEOS-PDMS), g-C3N4, and organic cellulose phases to the total mass, this Ms value is more than sufficient for the composite structure to exhibit a sensitive and stable orientation response toward an external magnetic field (Čebela et al. 2025; Nazir et al. 2024).

On the other hand, the low remanent magnetization (Mr = 1.36 emu/g) and coercivity (Hc = 14.51 Oe) values determined at zero applied field (H = 0), together with the notably low squareness ratio (Mr/Ms = 0.044), confirm the superparamagnetic-like stability of the material (Čebela et al. 2025; Nazir et al. 2024). This low remanence character offers a significant advantage in photocatalytic processes, as it prevents the agglomeration of particles on the fabric fibers through magnetostatic interactions once the external magnetic field is removed (Abu-Dief and Abdel-Fatah 2018). The VSM findings, together with the magnetic attraction photographs presented in the inset of Figure 6, confirm that the synthesized superhydrophobic and photocatalytic hybrid fabrics can be easily separated from the liquid phase within seconds using an external magnet after the reaction, without any mass loss.

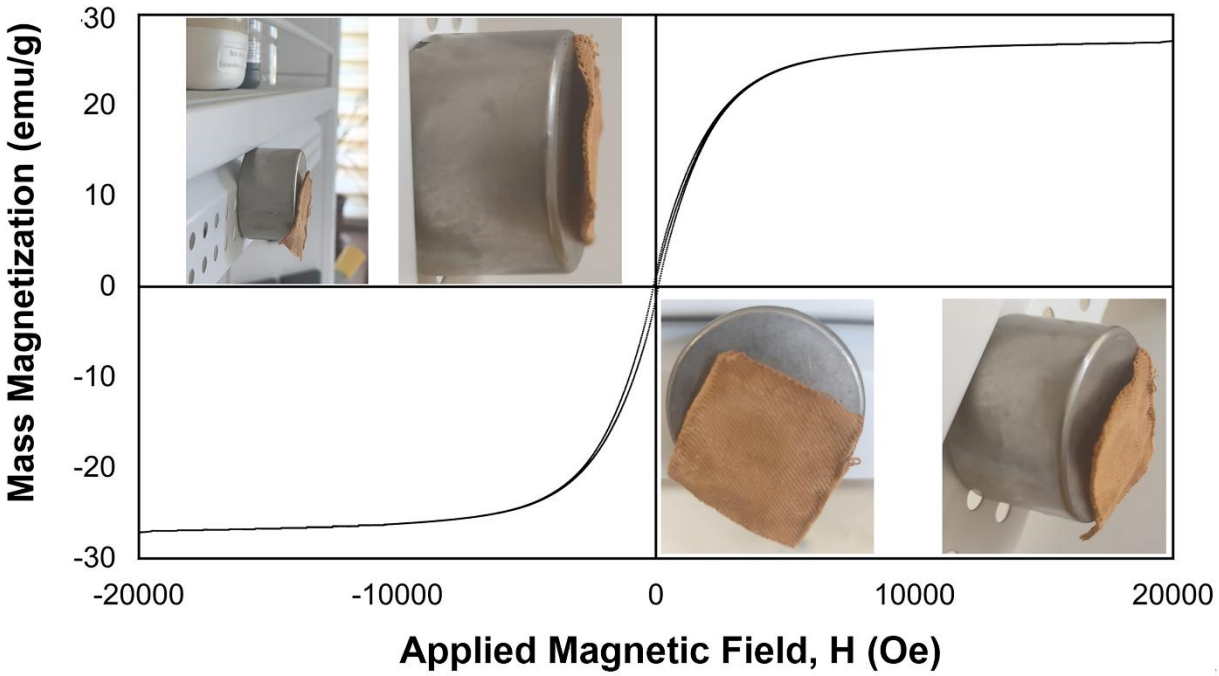


Figure 6. M-H hysteresis loop of the $BiFeO_3$@g-C_3N_4/TEOS-PDMS-coated cotton fabric measured at room temperature (298 K); inset photographs demonstrate the magnetic attraction and recoverability of the coated fabric using an external magnet

3.2. Surface Wettability and Superhydrophobic Performance

The surface wettability characteristics of the developed cotton fabric samples coated with the $BiFeO_3$@g-C_3N_4/TEOS-PDMS hybrid coating were systematically analyzed using time-dependent static water contact angle (WCA) measurements. As demonstrated in Figure 7a and b, both the untreated pure cotton fabric and the fabric modified solely with the $BiFeO_3$@g-C_3N_4 nanocomposite demonstrated extreme hydrophilicity, rapidly absorbing water droplets upon contact. This behavior is attributable to the elevated surface energy engendered by the inherent hydroxyl groups present within the textile matrix. Moreover, the nanocomposites themselves are devoid of alkyl/siloxane functional groups, which would otherwise serve to reduce surface energy (Sutar et al., 2024). As illustrated in Figure 7c, which contains no nanomaterials and has been modified solely with a TEOS-PDMS silane matrix, a partial hydrophobic character of 127° was initially observed (at 15 s) due to the matrix's low surface energy. However, the polymeric network structure, devoid of hierarchical micro/nano-roughness support, proved incapable of impeding capillary seepage within the porous fiber structure of the cotton fabric over time. By the 90th second, the contact angle had diminished to 58°, and by the conclusion of 120 seconds, the droplet had entirely infiltrated the fabric. This gradual degradation clearly demonstrates that low surface energy alone is not sufficient; geometric micro/nano roughness is indispensable for achieving permanent superhydrophobicity (Cao et al., 2016).

In contrast, the optimised fabric sample coated with $BiFeO_3$@g-C_3N_4/TEOS-PDMS, as demonstrated in Figure 7d, exhibited superior superhydrophobic performance and high stability over time, successfully retaining the water droplet on the surface at an exceptionally high contact angle of 165° without losing its shape even after 120 seconds of exposure. The hierarchical micro/nano-structural roughness provided by the $BiFeO_3$@g-C_3N_4 nanocomposite minimised the actual liquid-solid contact area by creating stable air pockets beneath the droplet, thereby preventing water from seeping into the fabric via capillary forces. Concurrently, the low surface energy induced by the TEOS-PDMS network served to reinforce this phenomenon, thereby ensuring the establishment of a stable Cassie-Baxter wetting regime on the surface. The developed hybrid coating's fundamental design principle is formed by a synergistic combination of hierarchical roughness and low surface energy, which stabilises the sample's superhydrophobic properties (Ghadei et al., 2025).

The surface wettability characteristics and multi-liquid repellency performance of the developed coatings were systematically analyzed using various local liquids and through underwater immersion tests. The optimised fabric sample coated with the $BiFeO_3$@g-C_3N_4/TEOS-PDMS hybrid coating (see Figure 8a) exhibited a superior multi-liquid repellency performance, a result of the synergistic combination of both structural roughness and low surface energy. A range of aqueous droplets with varying viscosities and surface tensions, including water, tea, coffee,

cola, fruit juice and milk, were observed to be unable to spread on the surface due to an inability to form hydrogen bonds with the hydrophobic siloxane matrix. Consequently, these droplets retained their spherical shape at a high contact angle. This behavior serves to confirm that a stable Cassie-Baxter wetting regime has been established on the surface, and that the actual liquid-solid contact area has been minimised. Conversely, due to the coating's superoleophilic character—that is, the nonpolar surface's propensity to preferentially wet oil phases—a commercial olive oil droplet was rapidly absorbed by the fabric upon contact through strong van der Waals interactions with the nonpolar structure of the PDMS matrix (Li et al., 2019).

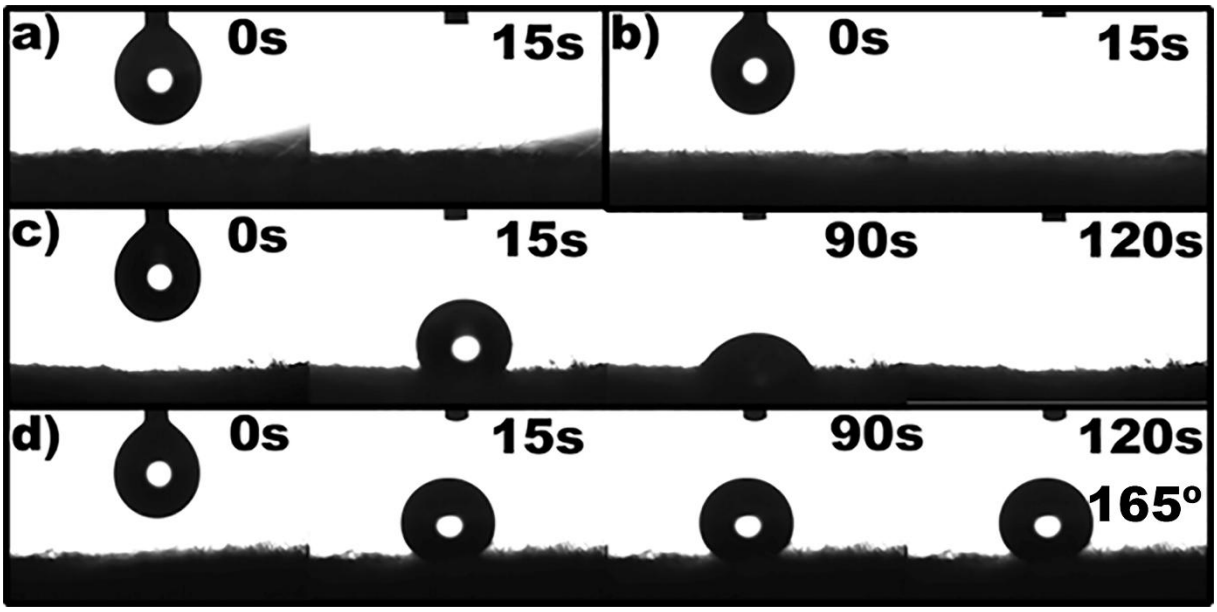


Figure 7. Optical photographs of static water contact angle (WCA) measurements on the investigated textile surfaces at 0, 90, and 120 s after water droplet deposition: (a) Untreated pristine cotton, (b) $BiFeO_3$@g-C_3N_4 modified cotton, (c) TEOS-PDMS coated cotton, and (d) hierarchical $BiFeO_3$@g-C_3N_4/TEOS-PDMS hybrid coated cotton fabric.

In order to quantitatively verify the synergy between the components, the multi-liquid repellency performance of the control samples was examined comparatively. In the fabric sample that did not contain nanomaterials and was modified only with a TEOS-PDMS silane matrix (see Figure 8b), the matrix's low surface energy initially provided a partial hydrophobic character. However, this polymeric network structure, lacking the support of hierarchical micro/nano roughness, was unable to prevent the capillary penetration of various liquids over time, resulting in the liquids completely penetrating the fabric. Conversely, as demonstrated in Figures 8c and d, the fabric modified with the $BiFeO_3$@g-C_3N_4 nanocomposite and the untreated pure cotton fabric exhibited extreme hydrophilicity towards all types of liquids, absorbing the droplets upon contact. This hydrophilic behavior was consistently observed across all aqueous phases, regardless of the liquid type or viscosity. This observation serves to once again confirm the decisive role of surface energy.

The purpose of this experiment was to evaluate the underwater stability and interfacial behavior of the prepared hybrid coating. To this end, a fabric sample was secured to a glass surface and immersed in pure water. As demonstrated in Figure 8e, the fabric surface submerged in water exhibited a characteristic silvery, mirror-like appearance. This phenomenon, defined in the literature as the "plastron effect," stems from a continuous air layer trapped within the micro/nano-rough valleys formed by the cross-linked TEOS-PDMS matrix with its hierarchical structure. This stable air barrier has been shown to impede the penetration of water molecules into the fiber pores, thereby minimizing direct contact between the water and the solid surface. Concurrently, a silvery sheen emerges on the surface, attributable to total internal reflection occurring at the air-water interface (Shi et al., 2024; Cai et al., 2021). These visual findings confirm that the developed coating can maintain the Cassie-Baxter wetting regime not only under static conditions but also underwater.

The practical and industrial success of superhydrophobic textile surfaces is directly linked to their self-cleaning ability, which preserves surface quality. The self-cleaning performance of the developed fabric was simulated using coffee particles as an artificial contaminant and examined in comparison with untreated pure cotton fabric. As demonstrated in Figures 8f and g, following the deposition of coffee particles on the surfaces of both samples,

drops of pure water were applied. The water droplets applied to the untreated cotton fabric rapidly penetrated the fiber structure along with the coffee particles due to the surface's highly energetic hydrophilic nature, resulting in noticeable staining on the surface. Conversely, a wholly divergent behavior was observed on the surface of the hybrid-coated fabric. Water droplets, upon contact with the superhydrophobic fabric surface, exhibited a rapid rolling-off behavior, preserving their spherical shape without spreading across the surface. This phenomenon can be attributed to the minimal adhesion force between the solid and liquid, which ensures the droplets maintain their shape. During this dynamic rolling-off motion, the water droplets adsorbed the coffee particles on the surface and removed them via gravity before they could adhere to the fabric. Following the conclusion of the test, it was evident that the surface of the coated fabric remained immaculate. This behavior, known in nature as the "Lotus Effect" (Chen et al., 2019; Yang et al., 2019), is a characteristic feature of low-surface-energy surfaces with hierarchical nano/micro roughness. The stable Cassie-Baxter regime on the coated surface ensures that water droplets move away from the surface at a low sliding angle, and that dirt particles are easily removed (Foorginezhad and Asadnia, 2023; Acha et al., 2025). The findings confirm that the developed hybrid coating demonstrates superior stain resistance and effective self-cleaning performance.

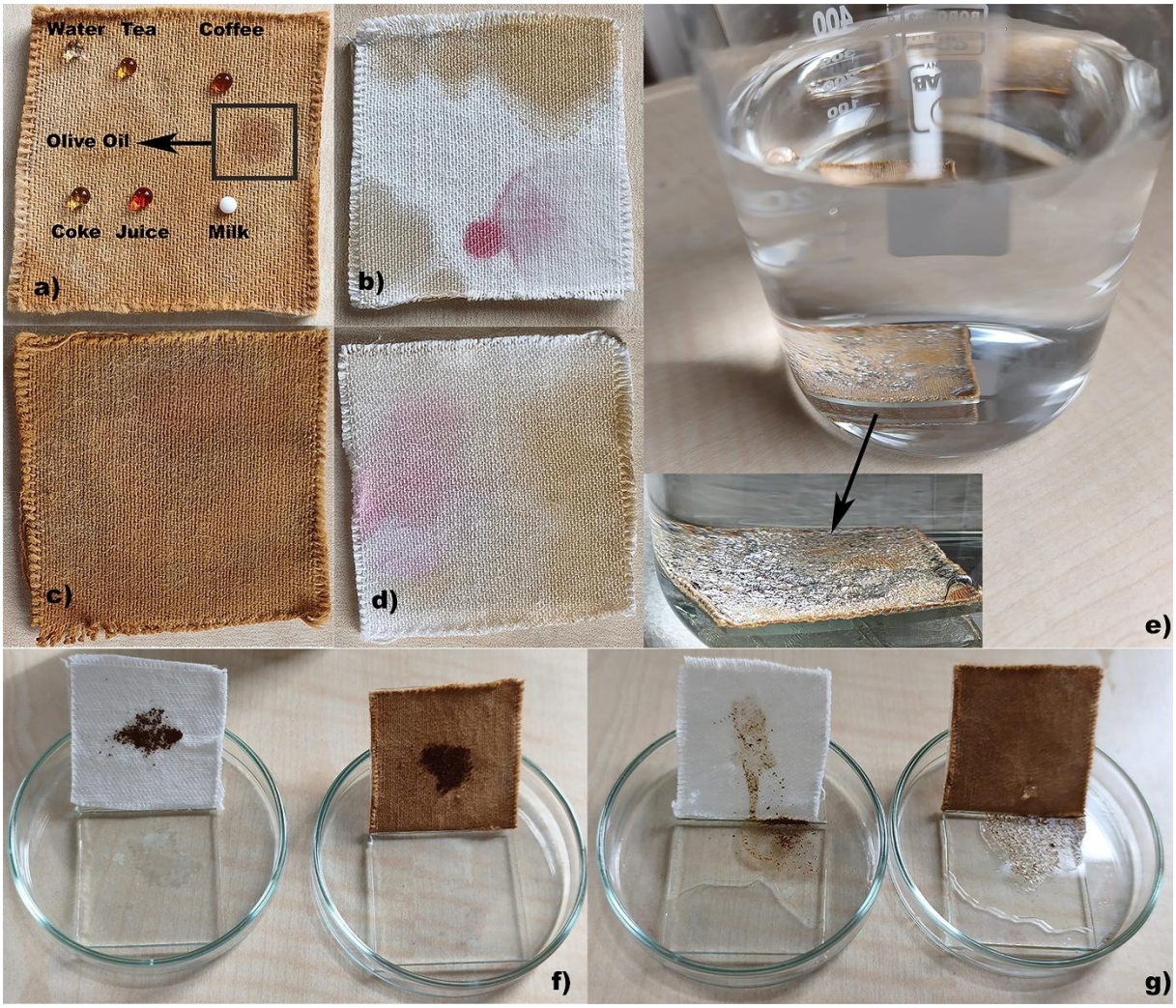


Figure 8. Wetting characteristics, underwater behavior, and self-cleaning performance of the samples: (a) Various liquid droplets on $BiFeO_3$@g-C_3N_4/TEOS-PDMS coated cotton fabric, (b) TEOS-PDMS coated cotton, (c) $BiFeO_3$@g-C_3N_4 modified cotton, (d) untreated pristine cotton fabric, (e) the bright silver mirror-like (plastron) effect of the optimized $BiFeO_3$@g-C_3N_4/TEOS-PDMS coating under water immersion, (f) coffee-contaminated untreated pristine cotton (left) and $BiFeO_3$@g-C_3N_4/TEOS-PDMS coated cotton (right) before rinsing, and (g) the same fabrics after rinsing, demonstrating complete stain removal on the coated fabric while the pristine cotton retained visible contamination.

3.3. Mechanical Durability and Chemical Stability

The sustainability of superhydrophobic textile surfaces in industrial applications is directly related to their interfacial resistance to various harsh chemical environments and mechanical stresses. In this study, the chemical stability and mechanical strength of the cotton fabric coated with the developed $BiFeO_3$@g-C_3N_4/TEOS-PDMS composite were systematically investigated. The alterations in the static water contact angle, as measured subsequent to chemical exposure tests, are illustrated in Figure 9a. The contact angle, which averages 165° under standard conditions (see Figure 9b), was measured at 155° after 24 hours of incubation in a pH 2 acidic environment. This indicates the relative resistance of the Si-O-Si siloxane network in the TEOS-PDMS matrix to acidic hydrolysis (Liang et al. 2026). The observation that the contact angle remained at 162° in a 3.5% NaCl salt solution - employed to investigate the effect of ionic strength - suggests that ionic penetration does not significantly compromise the coating's integrity. The contact angles measured following exposure to nonpolar organic solvents (toluene, DCM, and chloroform) remained well above the superhydrophobic threshold at 161°, 159°, and 158°, respectively, thus confirming the coating's high resistance to nonpolar environments. Notwithstanding the thermodynamic propensity of PDMS segments to dissolve in non-polar solvents, it is considered that the cross-linked siloxane network structure exerts a significant effect in preventing solvent-induced swelling and structural degradation (Abu Bakar et al. 2024; Foorginezhad and Asadnia 2023). Conversely, tests conducted in an environment with a pH of 12 revealed that the contact angle decreased to 129°, remaining below the threshold for superhydrophobic behavior. Si-O-Si bonds are more susceptible to nucleophilic attack by OH- ions in basic environments than in acidic environments. Consequently, the partial hydrolysis of the TEOS-derived silica network under alkaline conditions limits stability by reducing surface roughness and diminishing the density of low-surface-energy methyl groups (Liang et al. 2026; Eduok et al. 2021).

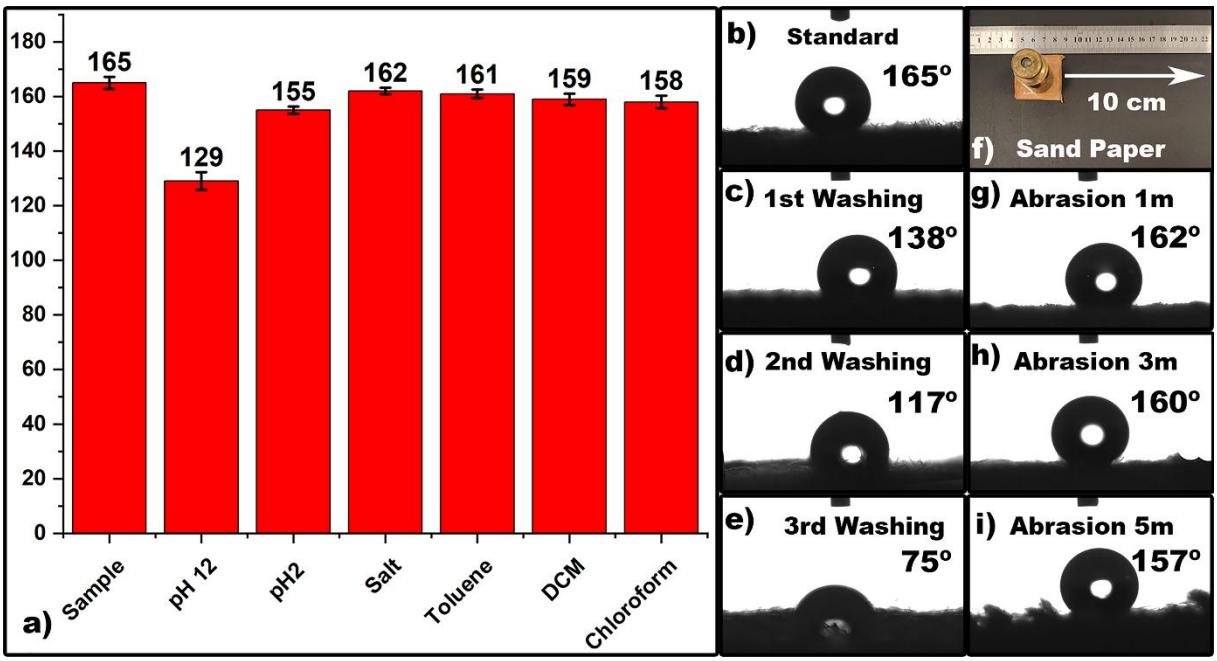


Figure 9. Chemical stability and mechanical durability of the optimized $BiFeO_3$@g-C_3N_4/TEOS-PDMS coated cotton fabric: (a) WCA variation after exposure to different chemical environments; (b) reference coating (WCA = 165°); (c–e) WCA values after the 1st, 2nd, and 3rd AATCC 61-1A washing cycles (~5, 10, and 15 equivalent home launderings); (f) sandpaper abrasion test setup; (g–i) retained WCA after cumulative abrasion distances of 1 m (162°), 3 m (160°), and 5 m (157°).

The coating's resistance to household washing cycles was evaluated based on the AATCC 61 No. 1A standard, in which each cycle is equivalent to five household washes. An analysis of the test results indicates that the contact angle decreased to 138° after the first wash cycle, to 117° after the second cycle, and to 75° at the end of the third cycle; by the completion of the fourth cycle, the superhydrophobic property had been completely lost (see Figure 9c, d, e). This observed gradual degradation is attributable to the combination of two primary factors: mechanical agitation and ball-impact stress during the washing processes weaken the physical integrity of the coating, while the alkaline detergent solution - consistent with the findings of the pH 12 test - partially hydrolyses the Si-O-Si bond network, thereby detaching the coating from the fabric fibers. Conversely, the coating's mechanical abrasion

resistance was evaluated along a straight-line path employing sandpaper abrasion tests (see Figure 9f). Depending on the specified abrasion distances, the contact angle was found to be 162° at the end of a 1 m cumulative abrasion distance (Figure 9g), 160° at 3 m (Figure 9h), and 157° even after completing the most severe abrasion stage at 5 m (Figure 9i). This demonstrates that the material perfectly retains its superhydrophobic character. The superior mechanical stability of the material has been attributed to the formation of strong covalent bonds between the cross-linked flexible siloxane network and the fabric fibers, as well as the inherently low coefficient of friction of PDMS (Zhang et al. 2018; Guo et al. 2019; Chen et al. 2022).

3.4. Gravity-Driven Oil-Water Separation Performance

In order to evaluate the oil-water separation performance and selective permeability of the synthesised $BiFeO_3$@g-C_3N_4/TEOS-PDMS-coated cotton fabric, a gravity-driven filtration setup was designed and tested. In this context, model organic phases lighter than water (n-hexane) and heavier than water (dichloromethane, DCM) were utilized to investigate the fabric's simultaneous superhydrophobic and superoleophilic characteristics under dynamic conditions.

As demonstrated in Figure 10a, in the filtration apparatus where the modified fabric was positioned horizontally, both oil-water mixtures were efficiently separated without the necessity for external energy input. When the n-hexane/water mixture – an organic phase lighter than water – was introduced into the system, the superoleophilic matrix instantaneously absorbed the oil phase and filtered it downward due to capillary forces, while the water phase was completely blocked on the fabric surface. In a similar manner, the DCM phase, which is denser than water, rapidly passed through the fabric pores due to the gravitational effect resulting from its high density, while the water phase was trapped in the upper layer throughout the filtration process. This superior bidirectional separation performance stems from the stable Cassie-Baxter air barrier, trapped by micron- and nano-scale roughness on the fabric surface, which exhibits strong hydrophobic resistance to water passage, and concurrently from the highly affine superoleophilic network, which rapidly wets the oil phase (Li et al. 2026).

Upon the passage of DCM (a heavy, dense oil phase) through the system, an elevated flux value of 8,928 $L \cdot m^{-2} \cdot h^{-1}$ and a separation efficiency of 99.2% were attained in the initial cycle. This outcome can be attributed to the synergy between the elevated hydrostatic pressure generated by gravity and the capillary attraction forces. In tests conducted with the n-hexane phase, which is lighter than water, the first-cycle flux was calculated to be 7,462.5 $L \cdot m^{-2} \cdot h^{-1}$, and the separation efficiency was 99.5%. The phenomenon of the high-density DCM phase flowing through the vertical pore network of the textile matrix at a higher hydrodynamic velocity is consistent with the dynamics of heavy/light oil filtration reported in the literature (Hou et al. 2025).

In order to assess the long-term industrial usability of the coating, the filtration process was repeated over 10 consecutive cycles. At the conclusion of the 10th cycle, the DCM flux had decreased to 8,191.6 $L \cdot m^{-2} \cdot h^{-1}$ (efficiency 98.3%), while the n-hexane flux had decreased to 6,939.8 $L \cdot m^{-2} \cdot h^{-1}$ (efficiency 98.7%) (Figure 10b, c). The observation that the decline in separation efficiency remained relatively limited for both oil systems suggests that the TEOS-PDMS matrix exerts a strong binding effect on the nanoparticles to the textile surface, thereby maintaining the structural stability of the coating under repeated use (Wang et al. 2024; Yan et al. 2026). This slight decrease in flow rates, observed as the cycle count increases, can be attributed to the slight capillary resistance (clogging) caused over time by micro-scale oil residues remaining in the fibers' micropores (Luo et al. 2026).

In addition to fixed filtration systems, the functionality of the developed smart textile is enhanced by the ferromagnetic character inherent in the $BiFeO_3$ nanoparticles within its structure. As demonstrated in Figure 10d, the modified fabric can be readily steered across the water surface through the application of an external magnetic field (magnet), enabling the selective collection of the free hydrophobic phase. The rapid absorption process that occurs the moment the fabric comes into contact with the oil phase on the water surface (Figure 10d) demonstrates that the developed matrix can function as a remotely controllable kinetic "active oil-capture interface," thus surpassing the limitations of static filtration.

As evidenced by the extant literature, gravity-driven oil collection concepts have been implemented using various systems. As demonstrated by Liu et al. (2023), jute fabric coated with PDMS/SiO_2 aerogel autonomously collected floating viscous oil without requiring additional energy input, through the synergistic effect of surface tension, gravity, and liquid pressure. The system exhibited a recovery efficiency of over 94% after 50 cycles. In contrast, Bayram (2025) demonstrated that cotton fabric modified with PLA/PCL nanofiber mats loaded with Fe_3O_4

nanoparticles not only achieved an efficiency exceeding 98% in gravity-driven oil-water separation but could also be guided to targeted locations using an external magnetic field. In this study, these concepts were integrated into a $BiFeO_3$@g-C_3N_4/TEOS-PDMS multicomponent system, thereby enabling superhydrophobic oil-water separation with over 99% efficiency, gravity-driven filtration, remotely guidable active oil collection via a magnetic field, and photocatalytic self-cleaning functions to be performed simultaneously on a single platform. The finding that the $BiFeO_3$ component exhibits both photocatalytic activity and ferromagnetic controllability in a simultaneous manner unequivocally differentiates the present study from analogous systems documented in the extant literature with respect to functional versatility.

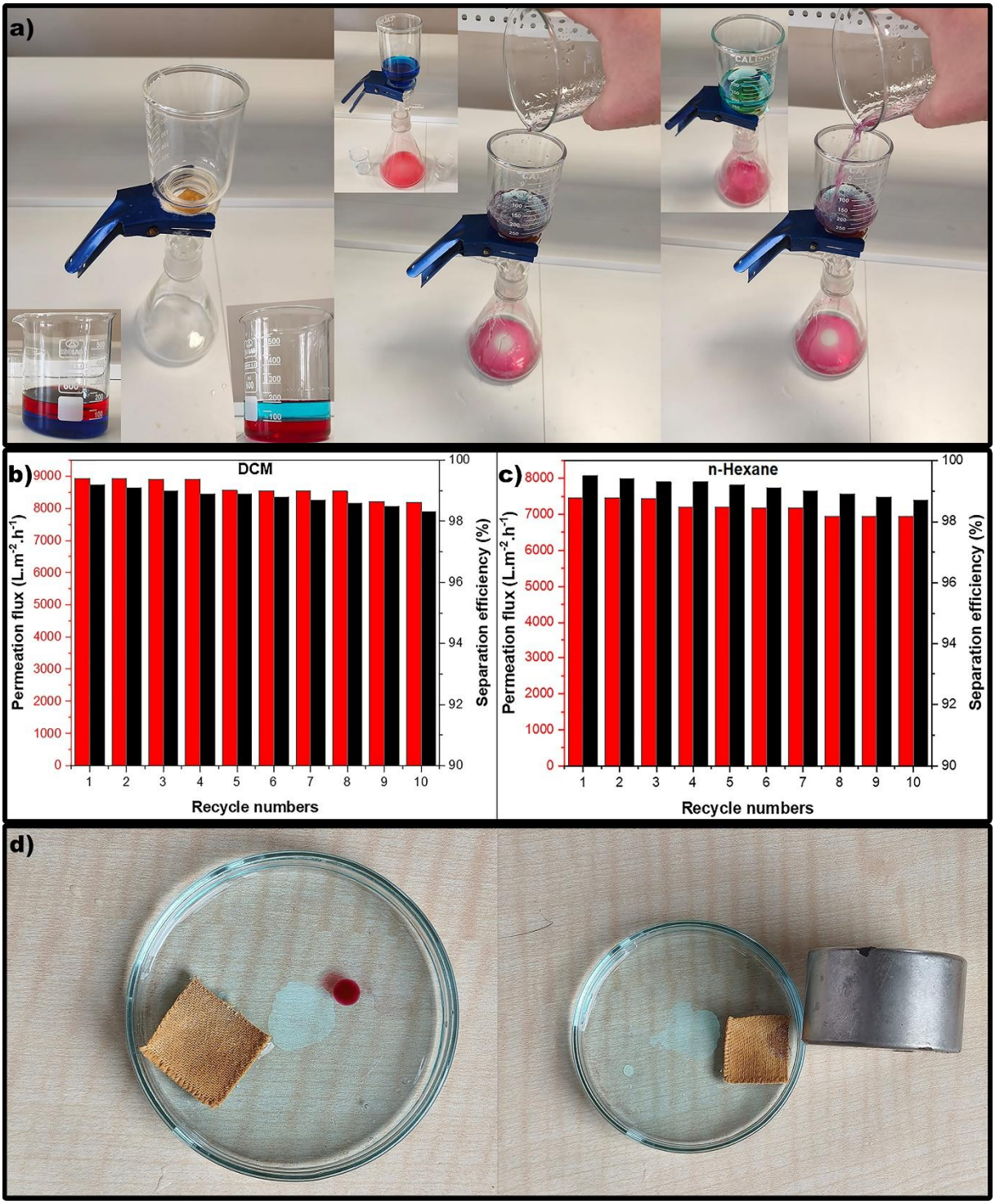


Figure 10. Multifunctional oil–water separation and magnetic responsiveness of the optimized $BiFeO_3$@g-C_3N_4/TEOS-PDMS coated cotton fabric: (a) gravity-driven separation of light oil (n-hexane) and heavy oil (DCM);

(b, c) cyclic permeation flux ($L \cdot m^{-2} \cdot h^{-1}$) and separation efficiency (%) over 10 consecutive recycles for DCM and n-hexane, respectively; (d) magnetic-driven selective oil absorption from the water surface via the ferromagnetic character of the embedded $BiFeO_3$ nanoparticles.

3.5. Photocatalytic Performance and Mechanism of $BiFeO_3$@g-C_3N_4/TEOS–PDMS-Coated Cotton Fabric

3.5.1. Photocatalytic Degradation Performance and Kinetics

The photocatalytic activity of the $BiFeO_3$@g-C_3N_4/TEOS-PDMS-coated cotton fabric was systematically evaluated using Rhodamine B (RhB, 1.25 mg/L) as a model organic pollutant under UVA and visible-light irradiation. As shown in Fig. 11a, direct photolysis of RhB was negligible under both irradiation conditions, with removal efficiencies of 6.23% and 15.66% under UVA and visible light, respectively, in the absence of the photocatalyst. The corresponding values for the uncoated cotton fabric were similarly low (7.25% and 16.05%, respectively), confirming that neither spontaneous photolysis nor the fabric substrate contributed meaningfully to dye removal. In contrast, the $BiFeO_3$@g-C_3N_4/TEOS-PDMS-coated cotton exhibited markedly enhanced photocatalytic performance, achieving RhB removal efficiencies of 77% and 83% after 70 min under UVA and visible-light irradiation, respectively. The superior activity under visible light can be attributed to the complementary photoresponsive properties of $BiFeO_3$ and g-C_3N_4. The narrow band gap of $BiFeO_3$ enables efficient visible-light harvesting, while the intimate interfacial coupling between $BiFeO_3$ and g-C_3N_4 promotes interfacial charge transfer and suppresses the recombination of photogenerated electron–hole pairs. Consequently, the enhanced availability and lifetime of photogenerated charge carriers facilitate the formation of reactive oxygen species (ROS), thereby accelerating RhB degradation.

To gain deeper insight into the reaction dynamics, the photodegradation kinetics were further investigated using the pseudo-first-order kinetic model derived from the Langmuir–Hinshelwood approach (Özdemir et al. 2022):

$$ln(C_0 / C_t) = k_{app} \cdot t \quad (4)$$

where C_0 and C_t denote the RhB concentrations after adsorption–desorption equilibrium and at irradiation time t, respectively, while kapp represents the apparent pseudo-first-order rate constant. As illustrated by the linear regression fits in Fig. 11b, the experimental data exhibit an excellent correlation with the pseudo-first-order model, yielding high R^2 values of 0.9984 and 0.9979 for UVA and visible-light irradiation, respectively. The corresponding kinetic parameters are systematically summarized in Table 2. The apparent rate constants were determined to be 0.0049 min^{-1} under UVA irradiation and 0.0058 min^{-1} under visible-light irradiation, while the initial reaction rates were calculated as 0.0128 and 0.0151 μM min^{-1}, respectively. The approximately 18% higher degradation rate under visible light is consistent with the enhanced RhB removal efficiency observed under the same conditions. Moreover, the high R^2 values of 0.9984 and 0.9979 for UVA and visible light, respectively, demonstrate an excellent correlation between the experimental data and the pseudo-first-order kinetic model.

Table 2. Pseudo-first-order photodegradation kinetic parameters of RhB under UVA and visible-light irradiation over the $BiFeO_3$@g-C_3N_4/TEOS-PDMS-coated cotton fabric.

Light Source	k_{app} (min^{-1})	r_0 (μM·min^{-1})	R^2
UVA	0.0049	0.0128	0.9984
Visible Light	0.0058	0.0151	0.9979

To identify the reactive species responsible for RhB degradation and provide experimental support for the proposed charge-transfer pathway, systematic scavenger experiments were subsequently performed (Fig. 11c) (Caglar et al., 2021). In the absence of scavengers, RhB removal efficiencies of 78% and 83% were obtained under UVA and visible-light irradiation, respectively. Upon addition of 2-propanol (IPA), a well-established •OH scavenger, the degradation efficiencies dramatically decreased to 9.00% and 10.00%, respectively. This pronounced inhibition clearly demonstrates that hydroxyl radicals (•OH) are the predominant reactive species governing RhB degradation. In comparison, the addition of L-ascorbic acid (LA), employed as a scavenger for superoxide radicals ($•O_2^-$), reduced the degradation efficiencies to 30.0% under UVA and 33.0% under visible-light irradiation, confirming the substantial contribution of $•O_2^-$ as a secondary reactive species. By contrast, the addition of EDTA-Na as a hole (h^+) scavenger resulted in only a moderate decrease in degradation efficiency, to 71.00% and 78.00% under UVA and visible light, respectively, indicating that photogenerated holes play a comparatively limited or indirect role in the overall RhB degradation process. Collectively, the scavenger results establish the relative contribution of the reactive species as $•OH > •O_2^- >> h^+$. The pronounced dominance of •OH, together with the

significant contribution of $\bullet O_2^-$, provides important experimental evidence for the involvement of strong oxidative and reductive reaction pathways in the $BiFeO_3$@g-C_3N_4 heterostructure. These findings are consistent with the charge-transfer pathway proposed in the subsequent mechanism discussion and support the feasibility of a direct Z-scheme-type charge-transfer mechanism capable of simultaneously retaining highly reducing electrons and strongly oxidizing holes.

Finally, the practical reusability and operational stability of the photocatalytic textile were assessed over five consecutive degradation cycles (Fig. 11d). The initial RhB removal efficiencies of 77.87% under UVA and 83.19% under visible light decreased only slightly to 73.54% and 79.58%, respectively, after five successive cycles. This corresponds to activity retentions of approximately 94.4% and 95.7% under UVA and visible-light irradiation, respectively. The limited loss of photocatalytic activity confirms the excellent cycling stability of the immobilized $BiFeO_3$@g-C_3N_4/TEOS-PDMS-cotton system. The high retention of photocatalytic performance can be attributed to the effective immobilization of the $BiFeO_3$@g-C_3N_4 nanostructure within the TEOS-PDMS-coated textile architecture, which minimizes catalyst loss during repeated operation while maintaining the structural integrity of the hybrid coating.

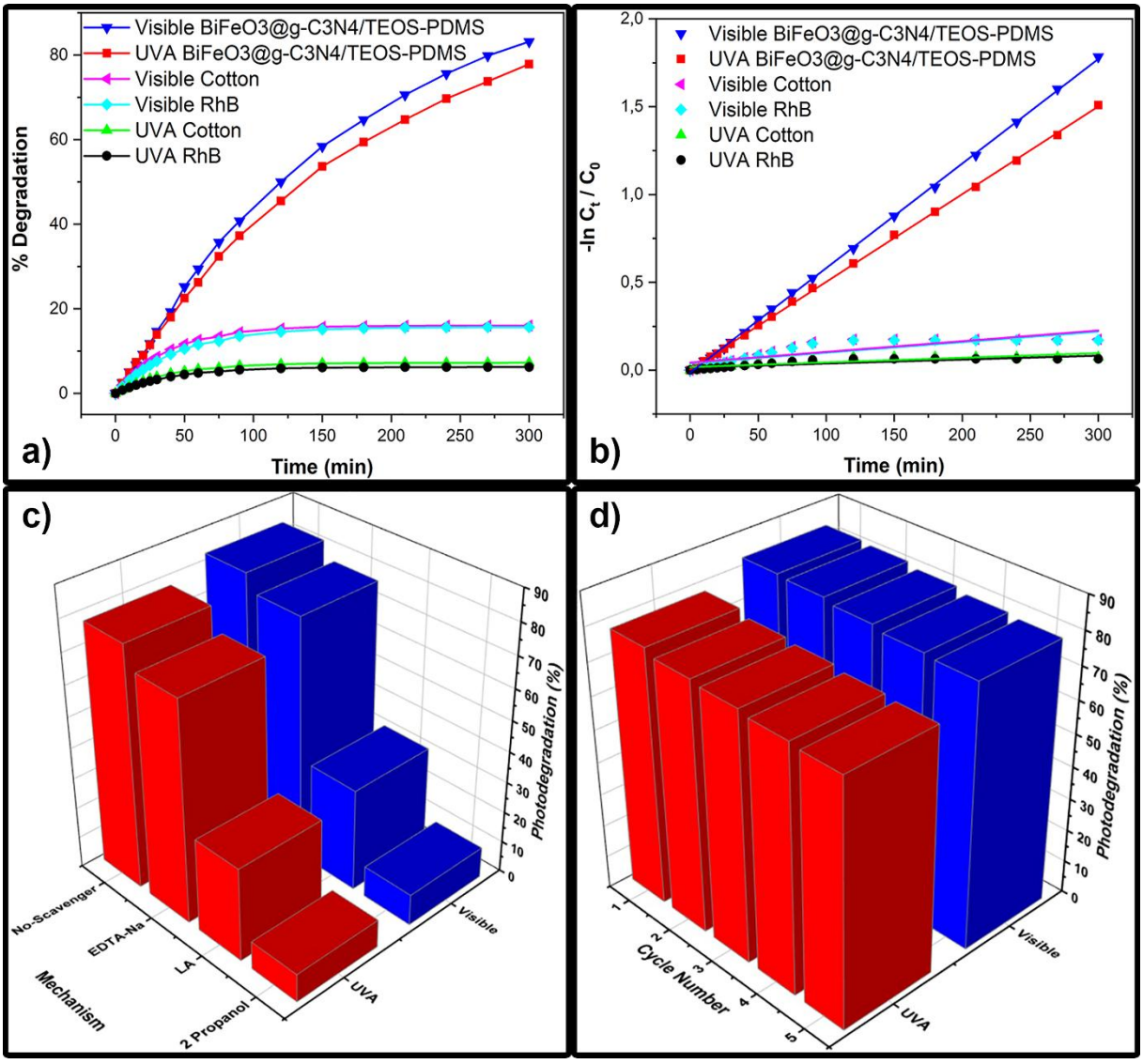


Figure 11. Photocatalytic decolorization performance of the $BiFeO_3$@g-C_3N_4/TEOS-PDMS-coated cotton fabric: (a) RhB removal efficiencies (%) under UVA and visible-light irradiation, (b) pseudo-first-order kinetic plots, (c) scavenger experiment results for identifying the reactive radical species involved in photocatalytic degradation, and (d) recyclability and stability tests over five consecutive cycles.

3.5.2. Photocatalytic Mechanism

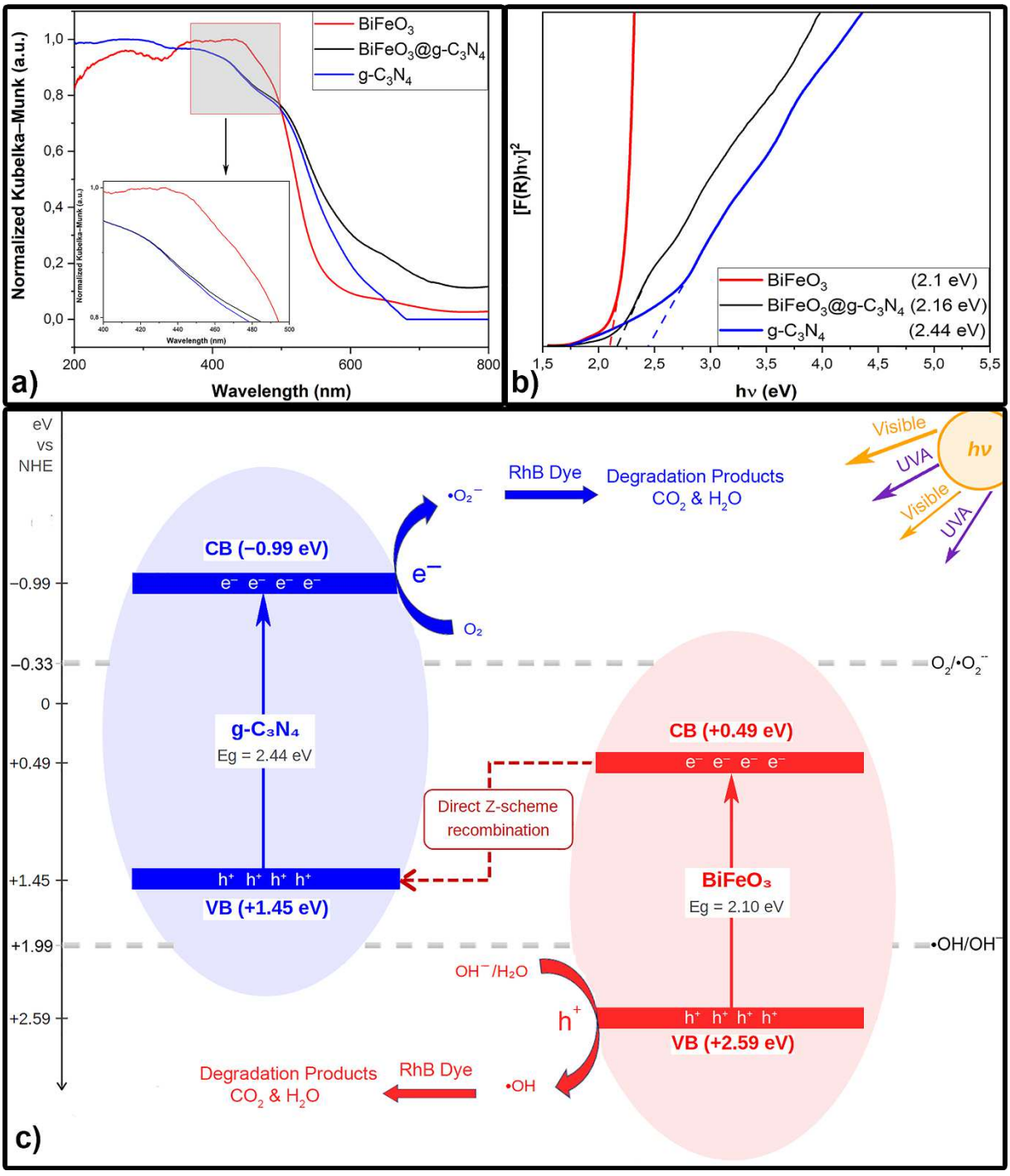


Figure 12. (a) UV–Vis DRS spectra of pristine $BiFeO_3$, pristine g-C_3N_4, and the $BiFeO_3$@g-C_3N_4 composite; inset: enlarged view (340–500 nm) showing the red-shift and enhanced absorbance of the composite relative to g-C_3N_4. (b) Corresponding Tauc plots showing the optical band-gap energies (Eg) of $BiFeO_3$ (2.10 eV), $BiFeO_3$@g-C_3N_4 (2.16 eV), and g-C_3N_4 (2.44 eV). (c) Proposed direct Z-scheme charge-transfer mechanism, showing CB/VB positions (vs. NHE), the interfacial recombination pathway, and $•O_2^-$/•OH radical generation responsible for RhB photodegradation.

The optical properties of pristine $BiFeO_3$, pristine g-C_3N_4, and $BiFeO_3$@g-C_3N_4/TEOS–PDMS-coated cotton fabric were investigated by UV–vis diffuse reflectance spectroscopy (DRS) (Fig. 12a). As shown in Fig. 12a, the absorption edge of pristine g-C_3N_4 extending into the blue/near-UV region (~450 – 500 nm) exhibits a noticeable red-shift toward the visible region upon composite formation. Furthermore, the enlarged view (340 – 500 nm) inset in Fig. 12a clearly demonstrates the enhanced normalized absorbance of the $BiFeO_3$@g-C_3N_4 composite over

pristine g-C_3N_4 within the visible-light range, confirming the successfully integrated optical response of the heterostructure. The reflectance data were converted to the Kubelka–Munk function using [$F(R\infty)=(1-R)^2/2R$] and the optical band-gap energies (Eg) were estimated using the Tauc relation, [$F(R\infty)\ h\nu)^2 = B(h\nu-Eg)$] assuming a direct allowed transition (Caglar et al. 2021a, 2021b). As shown in Fig. 12b, the Eg values were determined by extrapolating the linear regions of the corresponding Tauc plots to the photon-energy axis. The calculated band-gap energies were 2.10 eV for $BiFeO_3$, 2.44 eV for g-C_3N_4, and 2.16 eV for the $BiFeO_3$@g-C_3N_4 composite, respectively. Notably, the band gap of the composite lies between those of the pristine components and is closer to that of $BiFeO_3$, indicating that interfacial electronic interactions between $BiFeO_3$ and g-C_3N_4 modify the optical transition characteristics of the individual phases. This intermediate band-gap value further suggests effective electronic coupling at the $BiFeO_3$/g-C_3N_4 heterointerface.

The band-edge positions of $BiFeO_3$ and g-C_3N_4 were estimated using the electronegativity-based empirical approach (Ammar et al. 2024):

$$X(A_mB_nC_l) = \sqrt[m+n+l]{X_A^m X_B^n X_C^l} \quad (5)$$

where (X) represents the absolute electronegativity of the semiconductor, and (m), (n), and (l) denote the stoichiometric coefficients of the constituent elements. The valence-band (VB) and conduction-band (CB) edge positions were then estimated according to:

$$E_{VB} = X - E_e + 0.5E_g \quad (6)$$

$$E_{CB} = E_{VB} - E_g \quad (7)$$

where Ee is the energy of free electrons on the hydrogen scale (4.5 eV). Using the absolute electronegativity values of 6.04 and 4.73 eV for $BiFeO_3$ and g-C_3N_4, respectively, together with the experimentally determined optical band-gap energies, the VB and CB positions were estimated to be +2.59/+0.49 eV for $BiFeO_3$ and +1.45/−0.99 eV for g-C_3N_4. These calculated band-edge positions provide a useful energetic framework for interpreting the interfacial charge-transfer behavior of the $BiFeO_3$@g-C_3N_4 heterostructure.

Based on the optical, band-structure, and radical-scavenging results, a plausible charge-transfer mechanism for the enhanced photocatalytic activity of the $BiFeO_3$@g-C_3N_4 heterostructure is proposed and schematically illustrated in Fig. 12c. Upon UVA or visible-light irradiation, both $BiFeO_3$ and g-C_3N_4 can be photoexcited, generating electron–hole pairs when the incident photon energy exceeds their respective band-gap energies. In a conventional type-II charge-transfer configuration, the photogenerated electrons would preferentially migrate toward the lower-energy CB of $BiFeO_3$, while the holes would accumulate in the VB of g-C_3N_4. However, this pathway is inconsistent with the experimentally observed reactive-species formation. In particular, the relatively positive CB potential of $BiFeO_3$ (+0.49 eV) is thermodynamically insufficient for the reduction of dissolved O_2 to $\bullet O_2^-$, whose standard redox potential is approximately −0.33 eV. Likewise, the relatively positive VB potential of g-C_3N_4 (+1.45 eV) provides insufficient oxidation power for efficient •OH generation from H_2O/OH^-. Therefore, a conventional type-II charge-transfer pathway cannot satisfactorily account for the simultaneous formation of $\bullet O_2^-$ and •OH observed experimentally.

Considering both the band-edge energetics and the scavenger results (**$\bullet OH > \bullet O_2^- >> h^+$**)., a **direct Z-scheme-type charge-transfer pathway** provides a more consistent interpretation of the photocatalytic behavior. Under irradiation, the photogenerated electrons in the CB of $BiFeO_3$ can undergo interfacial recombination with the photogenerated holes in the VB of g-C_3N_4. This selective recombination eliminates the less-reactive charge carriers while preserving the strongly reducing electrons in the CB of g-C_3N_4 (−0.99 eV) and the strongly oxidizing holes in the VB of $BiFeO_3$ (+2.59 eV). The retained electrons on g-C_3N_4 possess sufficient reduction potential to activate dissolved oxygen:

$$O_2 + e^-_{CB} \rightarrow \bullet O_2^- \quad (8)$$

while the strongly oxidizing holes on $BiFeO_3$ can promote the formation of hydroxyl radicals through oxidation of surface hydroxyl groups and/or water:

$$H_2O + h^+_{VB,} \rightarrow \bullet OH + H^+ \quad (9)$$

$$OH^- + h^+_{VB,} \rightarrow \bullet OH \quad (10)$$

The resulting $\bullet O_2^-$ and, predominantly, •OH radicals subsequently attack the conjugated structure of RhB, promoting successive oxidative degradation and ultimately yielding smaller molecular intermediates and mineralization products.

Overall, the combination of the calculated band-edge positions, the thermodynamic limitations of a conventional type-II pathway, and the radical-scavenging results strongly supports a direct Z-scheme-type charge-transfer mechanism for the $BiFeO_3$@g-C_3N_4 heterostructure. Such a charge-transfer configuration preserves the highly reducing electrons of g-C_3N_4 and the strongly oxidizing holes of $BiFeO_3$, thereby enabling the concurrent generation of $\bullet O_2^-$ and •OH and providing a plausible explanation for the enhanced RhB degradation under both UVA and visible-light irradiation.

4. Conclusions

In this study, a fluorine-free, eco-friendly $BiFeO_3$@g-C_3N_4/TEOS-PDMS hybrid-coated smart cotton fabric platform, possessing superior superhydrophobic/superoleophilic wettability, magnetically guidable functionality, and visible-light-active photocatalytic self-cleaning capability, was successfully developed for advanced environmental remediation applications. The integration of the synthesised magnetic perovskite $BiFeO_3$ and polymeric g-C_3N_4 semiconductors was anchored to the textile fibers with high mechanical strength via the cross-linked network structure of the TEOS-PDMS siloxane matrix.

It is evident that the developed hybrid textile matrix has exhibited a separation efficiency that exceeds 99%, as well as superior permeation flow for both organic phases lighter than water (n-hexane) and heavier-than-water (DCM) organic phases in gravity-driven filtration systems. This is attributable to the water contact angle exceeding 150° and the stable Cassie-Baxter air barrier. Beyond the limits of conventional filtration, it has been established that the structure's ferromagnetic nature enables the fabric sample to function as an active component in the autonomous remediation of the environment, through its utilisation as a remotely controllable kinetic "oil-trapping interface" on the water surface, facilitated by the application of an external magnetic field.

More importantly, a correlated analysis of UV-Vis DRS absorption spectra, XPS valence band measurements, and radical scavenger experiments has clearly demonstrated that the system transfers photo-excited charge carriers via the Direct Z-Scheme mechanism. It is evident that the employment of this specific transfer mode has yielded highly efficient Rhodamine B (RhB) decolorisation under both visible light (83%) and UVA irradiation (77%), while concurrently ensuring the preservation of the strong redox potentials of the components. Furthermore, the identification of the primary reactive species as •OH and $\bullet O_2^-$ radicals has been substantiated. This multifunctional textile platform, which largely retains its performance and structural integrity even after 10 consecutive filtration and 5 photocatalysis cycles, distinctly stands out from its single-function counterparts in the literature in terms of functional versatility. It thus offers an environmentally friendly and sustainable alternative for industrial wastewater treatment and the autonomous cleanup of oil spills. Subsequent studies directed towards enhancing resistance to alkaline environments and evaluating system performance under real-world industrial wastewater scenarios will serve to further strengthen the practical applicability of this platform.

References

Abou Elmaaty TM, Elsisi H, Elsayad G, Elhadad H, Plutino MR (2022) Recent advances in functionalization of cotton fabrics with nanotechnology. Polymers 14(20):4273. https://doi.org/10.3390/polym14204273

Abtew MA, Dejene BK, Atalie D, Bajya M (2026) Advanced surface functionalization for smart, flexible and multi-threat impact resistance protective textiles and composites. Defence Technology. https://doi.org/10.1016/j.dt.2026.01.009

Abu Bakar NH, Wan Ismail WN, Mohd Yusop H, Mohd Zulkifli NF (2024) Synthesis of a water-based TEOS-PDMS sol-gel coating for hydrophobic cotton and polyester fabrics. New J Chem 48(2):933-950. https://doi.org/10.1039/d3nj03206j

Abu-Dief AM, Abdel-Fatah SM (2018) Development and functionalization of magnetic nanoparticles as powerful and green catalysts for organic synthesis. Beni-Suef University J Basic Appl Sci 7(1):55–67. https://doi.org/10.1016/j.bjbas.2017.05.008

Acha F, Egbebunmi D, Ahmadu S, Ojuolape A, Egbosiuba T (2025) Recent advances in bio-inspired superhydrophobic coatings utilizing hierarchical nanostructures for self-cleaning and anti-icing surfaces. Physchem 5(4):48. https://doi.org/10.3390/physchem5040048

Al-Shaeli M, Al-Juboori RA, Wang H, Ladewig B, Alsalhy QF, Zhang J (2026) Improving fouling resistance of polyvinylidene fluoride membrane with mono-hydroxyl poly(dimethylsiloxane) (PDMS-OH) grafted silica nanoparticles. Chem Eng J Adv 25:100991. https://doi.org/10.1016/j.ceja.2025.100991

Ammar SH, Ali F, Hadi H, Jabbar ZH (2024) Visible-light-induced photodegradation of ofloxacin antibiotic by facile assembled BiFeO3/Bi-modified g-C3N4 heterojunctions. Mater Sci Semicond Process 171:108026. https://doi.org/10.1016/j.mssp.2023.108026

Badawi NM, Batoo KM, Hussain S, Kasi R (2023) Design and characterization of electroconductive graphene-coated cotton fabric for wearable electronics. Coatings 13(3):546. https://doi.org/10.3390/coatings13030546

Bayram F (2025) Preparation of Superhydrophobic Cotton Textile Modified with Magnetic Nanoparticle-Loaded PLA/PCL Nanofiber Mats for Efficient Oil-Water Separation. Fibers Polymers 26:4857–4877. https://doi.org/10.1007/s12221-025-01125-6

Benisti I, Shaik F, Xing Z, Ben-refael A, Amirav L, Paz Y (2021) The effect of Pt cocatalyst on the performance and transient IR spectrum of photocatalytic g-C3N4 nanospheres. Appl Surf Sci 542:148432. https://doi.org/10.1016/j.apsusc.2020.148432

Bian J, Huang C, Zhang RQ (2016) Graphitic carbon nitride film: An emerging star for catalytic and optoelectronic applications. ChemSusChem 9(19):2723-2735. https://doi.org/10.1002/cssc.201600863

Caglar B, Guner EK, Ozdokur KV, Ozdemir AO, İçer F, Caglar S, Doğan B, Beşer BM, Çırak Ç, Tabak A, Ersoy S (2021a) Application of BiFeO3 and Au/BiFeO3 decorated kaolinite nanocomposites as efficient photocatalyst for degradation of dye and electrocatalyst for oxygen reduction reaction. J Photochem Photobiol A Chem 418:113400. https://doi.org/10.1016/j.jphotochem.2021.113400

Caglar B, İçer F, Özdokur KV, Caglar S, Özdemir AO, Guner EK, Beşer BM, Altay A, Çırak Ç, Doğan B, Tabak A (2021b) A novel amperometric H2O2 biosensor constructed by cress peroxidase entrapped on BiFeO3 nanoparticles. Mater Chem Phys 262:124287. https://doi.org/10.1016/j.matchemphys.2021.124287

Cai Y, Bing W, Chen C, Chen Z (2021) Gaseous plastron on natural and biomimetic surfaces for resisting marine biofouling. Molecules 26(9):2592. https://doi.org/10.3390/molecules26092592

Cao C, Ge M, Huang J, Li S, Deng S, Zhang S, Chen Z, Zhang K, Al-Deyab SS, Lai Y (2016) Robust fluorine-free superhydrophobic PDMS–ormosil@fabrics for highly effective self-cleaning and efficient oil–water separation. J Mater Chem A 4(31):12179–12187. https://doi.org/10.1039/C6TA04420D

Čebela M, Šenjug P, Zagorac D, Popov I, Zagorac J, Rosić M, Pajić D (2025) Synthesis, structural and magnetic properties of $BiFeO_3$ substituted with Ag. Materials, 18(7):1453. https://doi.org/10.3390/ma18071453

Chauhan SK, Kumar A, Verma NK, Jena P, Mahanti B, Patel SKS (2025) R3c to P1 phase transition in Nd3+/Gd3+ co-doped BiFeO3 nanoparticles: Enhanced magnetic and photocatalytic properties. Mater Sci Eng B 317:118170. https://doi.org/10.1016/j.mseb.2025.118170

Chen C, Li Z, Hu Y, Huang Q, Li X, Qing Y, Wu Y (2022) Rosin acid and SiO2 modified cotton fabric to prepare fluorine-free durable superhydrophobic coating for oil-water separation. J Hazard Mater 440:129797. https://doi.org/10.1016/j.jhazmat.2022.129797

Chen T, Hong J, Peng C, Chen G, Yuan C, Xu Y, Zeng B, Dai L (2019) Superhydrophobic and flame retardant cotton modified with DOPO and fluorine-silicon-containing crosslinked polymer. Carbohydr Polym 208:14–21. https://doi.org/10.1016/j.carbpol.2018.12.023

Deeksha, Kour P, Ahmed I, Haldar KK, Yadav CS, Sharma SK, Yadav K (2023) BiFeO3/g-C3N4/f-CNF ternary nanocomposite as an efficient photocatalyst for methylene blue dye degradation under solar light irradiation. J Alloys Compd 960:171073. https://doi.org/10.1016/j.jallcom.2023.171073

Deng Y, Peng C, Dai M, Lin D, Ali I, Alhewairini SS, Zheng X, Chen G, Li J, Naz I (2020) Recent development of super-wettable materials and their applications in oil-water separation. J Clean Prod 266:121624. https://doi.org/10.1016/j.jclepro.2020.121624

Diao H, Han Y, Shi S, Hu T, Ma K, Wang X (2026) Sustainable synthesis of ZnO nanocoating on cotton fabric via solid-state conversion for UV and antimicrobial protection. Ind Crops Prod 245:123275. https://doi.org/10.1016/j.indcrop.2026.123275

Eduok U, Faye O, Szpunar J, Khaled M (2021) Effect of silylating agents on the superhydrophobic and self-cleaning properties of siloxane/polydimethylsiloxane nanocomposite coatings on cellulosic fabric filters for oil-water separation. RSC Adv 11(16):9586–9599. https://doi.org/10.1039/d0ra10565a

El Mchaouri M, Mallah S, Abouhajjoub D, Boumya W, Elmoubarki R, Essadki A, Barka N, Elhalil A (2025) Engineering TiO2 photocatalysts for enhanced visible-light activity in wastewater treatment applications. Tetrahedron Green Chem 6:100084. https://doi.org/10.1016/j.tgchem.2025.100084

El-Shishtawy RM, Asiri AM, Abdelwahed NAM, Al-Otaibi MM (2011) In situ production of silver nanoparticle on cotton fabric and its antimicrobial evaluation. Cellulose 18(1):75-82. https://doi.org/10.1007/s10570-010-9455-1

Ennadi B, Rachid Y, Titchou FE, Errami M, Samir B, Zazou H, Hamdani M, Akbour RA (2026) Integrated coagulation-flocculation and column adsorption processes for efficient textile wastewater treatment. Process Saf Environ Prot 206:108264. https://doi.org/10.1016/j.psep.2025.108264

Esmaili-Nasrabadi F, Nasseri MA, Ghadirian M, Ghadirian F, Nasseh N (2026) A novel ternary heterojunction BiFeO3/UiO-66-NH2/BiOI photocatalyst for efficient visible-light-induced photodecomposition of metronidazole: Artificial intelligence-assisted modeling and optimization. J Environ Chem Eng 14(5):123620. https://doi.org/10.1016/j.jece.2026.123620

European Chemicals Agency (ECHA) (2023) Annex XV restriction report: Proposal for a restriction: Per- and polyfluoroalkyl substances (PFASs) (Version 2). https://echa.europa.eu/registry-of-restriction-intentions/-/dislist/details/0b0236e18663449b

Fan Y, Zhou J, Zhang J, Lou Y, Huang Z, Ye Y, Jia L, Tang B (2018) Photocatalysis and self-cleaning from g-C3N4 coated cotton fabrics under sunlight irradiation. Chem Phys Lett 699:146-154. https://doi.org/10.1016/j.cplett.2018.03.048

Feng F, Hong C, Ma J, Wang W, Li X, Hu J, Wang L, Zhang J, Zhao Z, Qu M, Zhao M (2026) Development of a new nitrogen-phosphorus synergistic flame-retardant system based on melamine and its application in cotton fabrics. Surf Interfaces 87:108880. https://doi.org/10.1016/j.surfin.2026.108880

Foorginezhad S, Asadnia M (2023) Superhydrophobic Al2O3/MMT-PDMS coated fabric for self-cleaning and oil–water separation application. Langmuir 39(50):18311–18326. https://doi.org/10.1021/acs.langmuir.3c02325

Fu S, Zhou H, Wang H, Ding J, Liu S, Zhao Y, Niu H, Rutledge GC, Lin T (2018) Magnet-responsive, superhydrophobic fabrics from waterborne, fluoride-free coatings. RSC Adv 8(2):717-723. https://doi.org/10.1039/c7ra10941e

Ghadei SK, Sankaran KJ, Sakthivel R (2025) Hybrid nano-interfacial engineering of special-wettable surfaces for advanced oil/water separation: Multifunctional strategies and future directions. Results Surf Interfaces 19:100526. https://doi.org/10.1016/j.rsurfi.2025.100526

Ghosh T, Jang NY, Kim T, Kim J (2025) Functional coatings for textiles: Advancements in flame retardancy, superhydrophobicity, and antimicrobial properties. J Ind Eng Chem (in press). https://doi.org/10.1016/j.jiec.2025.04.001

Glažar D, Tomšič B, Jerman I, Chouhan RS, Šuligoj A, Zorc M, Pintar A, Kovač J, Krajnc A, Ruiz-Zepeda F, Simončič B (2026) Surface-engineered Ag/TiO2/graphitic carbon nitride nanocomposites on cotton textiles for multifunctional photocatalytic, UV shielding, and antibacterial performance. Appl Surf Sci 721:165446. https://doi.org/10.1016/j.apsusc.2025.165446

Golubchikov D, Oleynichenko K, Murashko A, Efremov Y, Safaryan S, Pereira FDAS, Nifontova G, Solovieva A, Shpichka A, Timashev P (2025) Tuning poly(dimethylsiloxane) hydrophilization and coating stability via the optimization of polyethylene glycol molecular weight. Polymers 17(24):3296. https://doi.org/10.3390/polym17243296

Gomez-Iriarte GA, Pentón-Madrigal A, de Oliveira LAS, Sinnecker JP (2022) XPS study in BiFeO3 surface modified by argon etching. Materials 15(12):4285. https://doi.org/10.3390/ma15124285

Grosvenor AP, Kobe BA, Biesinger MC, McIntyre NS (2004) Investigation of multiplet splitting of Fe 2p XPS spectra and bonding in iron compounds. Surf Interface Anal 36(13):1564-1574. https://doi.org/10.1002/sia.1984

Guo H, Yang J, Xu T, Zhao W, Zhang J, Zhu Y, Wen C, Li Q, Sui X, Zhang L (2019) A robust cotton textile-based material for high-flux oil-water separation. ACS Appl Mater Interfaces 11(14):13704–13713. https://doi.org/10.1021/acsami.9b01108

Guo HY, Li B, Feng XQ (2016) Stability of Cassie-Baxter wetting states on microstructured surfaces. Phys Rev E 94(4):042801. https://doi.org/10.1103/PhysRevE.94.042801

Guo Y, Li J, Zhang J, Wang X (2024) Highly active BiFeO3-g-C3N4 S-scheme heterojunction with improved antibiotic degradation under visible-light: Revealing mechanism. Res Chem Intermed 50(8):3505-3521. https://doi.org/10.1007/s11164-024-05326-1

Hadhri M, D'Agostino A, Safarshargh A, Rosa RP, Rosace G, Trovato V (2026) Siloxane-based sol-gel coatings for fluorine-free water-repellent textiles. In: Guxho et al. (eds) Proceedings of the Joint International Conference: 5th Conference on Engineering and Entrepreneurship and 11th Textile Conference, vol 1324. Springer, pp 706-713. https://doi.org/10.1007/978-3-032-11085-5_62

Han Y, Yu Z, Yu P, Xia S, Chen J, Peng C (2026) Bio-based photocatalytic self-cleaning superhydrophobic cotton fabric based on rosin acid/TiO2: Efficient and recyclable application in oil-water separation. Int J Biol Macromol 364:152234. https://doi.org/10.1016/j.ijbiomac.2026.152234

Hao X, Zhou J, Cui Z, Wang Y, Wang Y, Zou Z (2018) Zn-vacancy mediated electron-hole separation in ZnS/g-C3N4 heterojunction for efficient visible-light photocatalytic hydrogen production. Appl Catal B Environ 229:41-51. https://doi.org/10.1016/j.apcatb.2018.02.006

Hou C, Gui Q, Song J, Fan Z (2025) Superhydrophobic cotton fabric and oil-water separation based on KH570 modified SiO_2 and fluorinated epoxy polymer. Colloids Surf A Physicochem Eng Asp 709:136167. https://doi.org/10.1016/j.colsurfa.2025.136167

Hu K, Tian J, Zhou Z, Zhao D, Guan X (2024) Direct Z-scheme photocatalytic systems based on vdW heterostructures for water splitting and CO2 reduction: Fundamentals and recent advances. Microstructures 4:2024021. https://dx.doi.org/10.20517/microstructures.2023.76

Hu X, Xing T, Wu H, Wei K, Souare M, Dong C (2025) Separation principles and strategies for an oil-water separation membrane with special wettability. Membranes 15(8):241. https://doi.org/10.3390/membranes15080241

Huang H, Jiang L, Yang J, Zhou S, Yuan X, Liang J, Wang H, Wang H, Bu Y, Li H (2023) Synthesis and modification of ultrathin g-C3N4 for photocatalytic energy and environmental applications. Renew Sustain Energy Rev 173:113110. https://doi.org/10.1016/j.rser.2022.113110

Jalandhara D, Kumar S, Kumar S, Rekha MM, Sharma SV, Kaushal S (2025) BiFeO3 as a next-generation photocatalyst: Bridging material design with environmental remediation. ChemPhysChem 26(10):e202401092. https://doi.org/10.1002/cphc.202401092

Jia J, Zhang Q, Li K, Zhang Y, Liu E, Li X (2023) Recent advances on g-C3N4-based Z-scheme photocatalysts: Structural design and photocatalytic applications. Int J Hydrogen Energy 48(1):196-231. https://doi.org/10.1016/j.ijhydene.2022.09.272

Kashem MNH, Nam S, Hillyer MB, Hassan F, Joshi S, Zimmerman T, Bruni G, King H, Hinchliffe D, Fang D (2026) Optimized one-pot room-temperature interfibrillar synthesis of silver nanoparticles using cotton fiber as

reductant for pathogen-resistant protective textiles. Clean Eng Technol 31:101178. https://doi.org/10.1016/j.clet.2026.101178

Katsina AU, Mihai S, Matei D, Cursaru DL, Şomoghi R, Nistor CL (2023) Construction of Pt@BiFeO3 xerogel-supported O-g-C3N4 heterojunction system for enhanced visible-light activity towards photocatalytic degradation of Rhodamine B. Gels 9(6):471. https://doi.org/10.3390/gels9060471

Kavitha G, Govindhan M, Premkumar S (2025) Dye pollution and its implications for human health, aquatic ecosystems, and sustainable wastewater treatment: A comprehensive review. J Water Process Eng 80:109071. https://doi.org/10.1016/j.jwpe.2025.109071

Keramea P, Zodiatis G, Sylaios G (2026) Analysis of major global oil spill incidents: Part 1-Environmental and ecological impacts. J Mar Sci Eng 14(2):153. https://doi.org/10.3390/jmse14020153

Kuroki S, Endo K, Maeda S, Chong DP, Duffy P (1998) Analysis of X-ray photoelectron spectra of silicon-based polymers by deMon density-functional calculations using model molecules. Polym J 30(2):142-148. https://doi.org/10.1295/polymj.30.142

Kurul F, Doruk B, Topkaya SN (2025) Principles of green chemistry: building a sustainable future. Discov Chem 2:68. https://doi.org/10.1007/s44371-025-00152-9

Lan H, Li L, An X, Liu F, Chen C, Liu H, Qu J (2017) Microstructure of carbon nitride affecting synergetic photocatalytic activity: Hydrogen bonds vs. structural defects. Appl Catal B Environ 204:49-57. https://doi.org/10.1016/j.apcatb.2016.11.022

Li D, Xu Y, Zhang S, Wang L (2025) Construction of a 1D/0D/2D BiFeO3/Ag/g-C3N4 Z-scheme heterojunction for enhanced visible light photocatalysis of methylene blue. RSC Adv 15(38):31508-31521. https://doi.org/10.1039/D5RA04825G

Li J, Chen C, Pan N, Wang L, Gao D (2026) Preparation and properties of superhydrophobic cotton fabric with micro-nano structure for self-cleaning, UV shielding and oil-water separation. Appl Mater Today 50:103243. https://doi.org/10.1016/j.apmt.2026.103243

Li X, Cao M, Shan H, Tezel FH, Li B (2019) Facile and scalable fabrication of superhydrophobic and superoleophilic PDMS-co-PMHS coating on porous substrates for highly effective oil/water separation. Chem Eng J 358:1101–1113. https://doi.org/10.1016/j.cej.2018.10.097

Liang Y, Xiong T, Luo R, Huang C, Chen Z, Wang S (2026) Chemical degradation mechanism of methyl-silica superhydrophobic coatings in acidic and alkaline environments. J Coat Technol Res. https://doi.org/10.1007/s11998-026-01296-8

Liu F, Di D, Sun X, Wang X, Yang T, Wang M, Li J, Wang C, Li Y (2023) Superhydrophobic/superoleophilic PDMS/SiO_2 aerogel fabric gathering device for self-driven collection of floating viscous oil. Gels 9(5):405. https://doi.org/10.3390/gels9050405

Liu IC, Hu X, Fei B, Lee C, Fan S, Xin JH, Noor N (2024) Fluorine-free nanoparticle coatings on cotton fabric: Comparing the UV-protective and hydrophobic capabilities of silica vs. silica-ZnO nanostructures. RSC Adv 14(7):4301-4314. https://doi.org/10.1039/d3ra08835a

Lu Y, Chen G, Zhang Y, Lv W, Zhang K, Lv Z, Huang Y (2026) Multifunctionalization of cotton fabric with ZnO for developing a superhydrophobic surface with breathability, UV resistance, antibacterial, and self-healing abilities. Colloids Surf A Physicochem Eng Asp 731:139091. https://doi.org/10.1016/j.colsurfa.2025.139091

Luo Y, Su W, Hossain M, Peng G, Liu L (2026) Rolling-Induced Phase Separation: A Dynamic Strategy for High-Performance Oil–Water Emulsion Filtration. Langmuir 42(14):9940–9950. https://doi.org/10.1021/acs.langmuir.6c00015

Ma X, Wang H, Chen Y, Fu L, Zhou J, Zhang L, Xing Z, Zhang Q, Xia L (2024) Application of Ag@g-C3N4/TiO2 cotton fabric flexible substrate with dual functionality: Photocatalytic reusability and SERS signal amplification for food safety detection. Appl Surf Sci 661:160068. https://doi.org/10.1016/j.apsusc.2024.160068

Maggay IV, Chang Y, Venault A, Dizon GV, Wu CJ (2021) Functionalized porous filtration media for gravity-driven filtration: Reviewing a new emerging approach for oil and water emulsions separation. Sep Purif Technol 259:117983. https://doi.org/10.1016/j.seppur.2020.117983

Majdoub A, Majdoub M, Zaitan H (2025) g-C3N4/MnO2 coated cotton fabric as effective dip-catalyst for organic dyes degradation via persulfate activation. Inorg Chem Commun 177:114447. https://doi.org/10.1016/j.inoche.2025.114447

Nazir MK, Javaid S, Afzal H, Taj MB, Baamer DF, Almasoudi A, Aldahiri RH, Ali OM, Khan MI, Ahmed MM, Shanableh A, Fernandez-Garcia J (2024) Synthesis, Magnetic, and Photocatalytic Activity of Polypyrrole-Based TiO_2-Fe Catalyst for Wastewater Treatment. Catalysts, 14(10):692. https://doi.org/10.3390/catal14100692

Noureen L, Wang Q, Humayun M, Shah WA, Xu Q, Wang X (2023) Recent advances in structural engineering of photocatalysts for environmental remediation. Environ Res 219:115084. https://doi.org/10.1016/j.envres.2022.115084

Özdemir AO (2026) Self-cleaning TiO2 nanoparticle-coated PET fabrics: Hydrophobicity and photocatalytic performance. J Text Inst 117(6):1338-1355. https://doi.org/10.1080/00405000.2025.2562658

Özdemir AO, Caglar B, Çubuk O, Coldur F, Kuzucu M, Guner EK, Doğan B, Caglar S, Özdokur KV (2022) Facile synthesis of TiO2-coated cotton fabric and its versatile applications in photocatalysis, pH sensor and antibacterial activities. Mater Chem Phys 287:126342. https://doi.org/10.1016/j.matchemphys.2022.126342

Park S, Huo J, Shin J, Heo KJ, Kalmoni JJ, Sathasivam S, Hwang GB, Carmalt CJ (2022) Production of an EP/PDMS/SA/AlZnO coated superhydrophobic surface through an aerosol-assisted chemical vapor deposition process. Langmuir 38(25):7825-7832. https://doi.org/10.1021/acs.langmuir.2c01060

Pawar SM, Patil SS, Patil AH, Landage SM, Vhanbatte SB, Patil AP, Patil PS (2025) Development of multifunctional cotton fabric via copper oxide nanoparticle deposition using the padding technique. Surf Interfaces 76:107823. https://doi.org/10.1016/j.surfin.2025.107823

Pei J, Li H, Zhuang S, Zhang D, Yu D (2023) Recent advances in g-C3N4 photocatalysts: A review of reaction parameters, structure design and exfoliation methods. Catalysts 13(11):1402. https://doi.org/10.3390/catal13111402

Pervez MN, Ilango AK, Jiang T, Talukder ME, Ehsan MN, Cai Y, Liang Y (2025) PFAS in the textile industry: Sources, fate, detection, and pathways toward sustainable remediation and regulation. Chem Eng J 522:168183. https://doi.org/10.1016/j.cej.2025.168183

Qin L, Wu Y, Ma Z, Li H, Lu S, Wang Z, Liu J, Dong M, Zhang Y (2023) Fluorine-free and highly durable superhydrophobic textiles for antifouling and anti-icing applications. ACS Appl Polym Mater 5(8):6278-6287. https://doi.org/10.1021/acsapm.3c00916

Rao C, Xin Y, Guo Z, Liu W (2026) Biomimetic multi-responsive superwettable materials for oil-water separation. Nano-Micro Lett 18:380. https://doi.org/10.1007/s40820-026-02222-8

Rasouli S, Rezaei N, Hamedi H, Zendehboudi S, Duan X (2021) Superhydrophobic and superoleophilic membranes for oil-water separation application: A comprehensive review. Mater Des 204:109599. https://doi.org/10.1016/j.matdes.2021.109599

Ren J, Wang Z, Wu J, Xiao J, Chu Z, Wang Y (2026) Bioinspired heterogeneous gradient-porous biomass aerogels for high-flux oil-water separation and self-healing. Sep Purif Technol 397:138121. https://doi.org/10.1016/j.seppur.2026.138121

Riabchykov M, Tkachuk O, Nazarchuk L, Motuziuk O (2024) Magnetic effects in textile fibers filled with nanoconstituents based on iron oxides. J Nat Fibers 21(1):2423211. https://doi.org/10.1080/15440478.2024.2423211

Sak G, Taşar Ş, Dursun G (2026) Organic pollutant degradation through photocatalysis: Progress, challenges, and sustainable solutions (Mini review). Appl Sci 16(1):204. https://doi.org/10.3390/app16010204

Samarasinghe LV, Muthukumaran S, Baskaran K (2025) Heterojunction photocatalysts for solar-driven wastewater treatment: Interfacial design, charge carrier dynamics, and advanced characterization techniques. J Water Process Eng 79:108960. https://doi.org/10.1016/j.jwpe.2025.108960

Saravanakumar K, Park CM (2021) Rational design of a novel LaFeO3/g-C3N4/BiFeO3 double Z-scheme structure: Photocatalytic performance for antibiotic degradation and mechanistic insight. Chem Eng J 423:130076. https://doi.org/10.1016/j.cej.2021.130076

Scheff T, Acha F, Diaz Armas N, Mead JL, Zhang J (2025) Tuning wetting properties through surface geometry in the Cassie-Baxter state. Biomimetics 10(1):20. https://doi.org/10.3390/biomimetics10010020

Shah SMH, Riaz S, Akbar A, Atiq S, Naseem S (2014) Effect of solvents on the ferromagnetic behavior of undoped $BiFeO_3$ prepared by sol-gel. IEEE Trans Magn 50(8):2200904. https://doi.org/10.1109/TMAG.2014.2309720

Shao L, Jiang D, Xiao P, Zhu L, Meng S, Chen M (2016) Enhancement of g-C3N4 nanosheets photocatalysis by synergistic interaction of ZnS microsphere and RGO inducing multistep charge transfer. Appl Catal B Environ 198:200-210. https://doi.org/10.1016/j.apcatb.2016.05.056

Shi Q, Fang K, Chen W, Tan Y, Zhang C (2024) Designing a superhydrophobic cotton fiber coating exploiting TiO2@g-C3N4 layered structure for augmented photocatalysis and efficient water-oil separation. Int J Biol Macromol 264:130596. https://doi.org/10.1016/j.ijbiomac.2024.130596

Si YH, Xia Y, Shang SK, Xiong XB, Zeng XR, Zhou J, Li YY (2018) Enhanced visible light driven photocatalytic behavior of BiFeO3/reduced graphene oxide composites. Nanomaterials 8(7):526. https://doi.org/10.3390/nano8070526

Sutar RS, Ekunde TA, Liu S, Kodag SG, Ekunde RA, Nagappan S, Sawant AS, Kim YH, Saji VS, Latthe SS (2024) Durable self-cleaning superhydrophobic cotton fabrics for wearable textiles. Ind Crops Prod 222:119717. https://doi.org/10.1016/j.indcrop.2024.119717

Türe H (2025) Simple preparation of biodegradable, superhydrophobic, and antifungal cellulose filter paper for efficient oil/water separation. Int J Biol Macromol 307:142371. https://doi.org/10.1016/j.ijbiomac.2025.142371

Upar DA, Gogoi D, Das MR, Naik B, Ghosh NN (2023) Facile synthesis of g-C3N4-exfoliated BiFeO3 nanocomposite: A versatile and efficient S-scheme photocatalyst for the degradation of various textile dyes and antibiotics in water. ACS Omega 8(41):38524-38538. https://doi.org/10.1021/acsomega.3c05357

Wakelyn PJ, Bertoniere NR, French AD, Thibodeaux DP, Triplett BA, Rousselle MA, Goynes WR, Edwards JV, Hunter L, McAlister DD, Gamble GR (2006) Cotton fiber chemistry and technology. CRC Press

Wang S, Hao W, Liu Z, Niu X, Wang L, Zhao Q (2026) Two-dimensional direct Z-scheme heterojunction photocatalysts for highly efficient energy conversion and chemical synthesis. ACS Nano 20(1):137-162. https://doi.org/10.1021/acsnano.5c18705

Wang W, Chen C, Li Z, Xu X, Li X, Qing Y, Cao Y, Wu Y (2024) A novel superhydrophobic cotton fabric constructed by rosin-based polymer and nano-hydroxyapatite for oil/water separation. Sep Purif Technol 349:127847. https://doi.org/10.1016/j.seppur.2024.127847

Wang Y, Li J, Song H, Wang F, Su X, Zhang D, Xu J (2025) Biomimetic superhydrophobic surfaces: From nature to application. Materials 18(12):2772. https://doi.org/10.3390/ma18122772

Wang Z, Lin Z, Shen S, Zhong W, Cao S (2021) Advances in designing heterojunction photocatalytic materials. Chin J Catal 42(5):710-730. https://doi.org/10.1016/S1872-2067(20)63698-1

Wei DW, Wei H, Gauthier AC, Song J, Jin Y, Xiao H (2020) Superhydrophobic modification of cellulose and cotton textiles: Methodologies and applications. J Bioresour Bioprod 5(1):1-15. https://doi.org/10.1016/j.jobab.2020.03.001

Wu Z, Fang K, Chen W, Zhao Y, Xu Y, Zhang C (2021) Durable superhydrophobic and photocatalytic cotton modified by PDMS with TiO2 supported bamboo charcoal nanocomposites. Ind Crops Prod 171:113896. https://doi.org/10.1016/j.indcrop.2021.113896

Xiang B, Sun Q, Zhong Q, Mu P, Li J (2022) Current research situation and future prospect of superwetting smart oil/water separation materials. J Mater Chem A 10(38):20190-20217. https://doi.org/10.1039/d2ta04469b

Xu T, Wang G, Liu Z, Deng N, Zhang X (2024) Construction of magnetically separable S-scheme BiFeO3/Cl-g-C3N4 heterostructure photocatalyst for simultaneous removal of Cr(VI) and tetracycline in aqueous solution: Performance and mechanism insight. J Catal 440:115821. https://doi.org/10.1016/j.jcat.2024.115821

Yan H, Yang H (2011) TiO2-g-C3N4 composite materials for photocatalytic H2 evolution under visible light irradiation. J Alloys Compd 509(4):L26-L29. https://doi.org/10.1016/j.jallcom.2010.09.201

Yan X, Du J, Wang K, Guo X, Jiang W, Jiao L, Shang B, Huang J, Gu S (2026) A facile, catalyst-free reactive polydimethylsiloxane coating toward multifunctional cotton textiles with superhydrophobicity, self-healing, oil-water separation, and secondary reactivity. Int J Biol Macromol 362:152158. https://doi.org/10.1016/j.ijbiomac.2026.152158

Yang M, Liu W, Jiang C, Xie Y, Shi H, Zhang F, Wang Z (2019) Facile construction of robust superhydrophobic cotton textiles for effective UV protection, self-cleaning and oil-water separation. Colloids Surf A Physicochem Eng Asp 570:172–181. https://doi.org/10.1016/j.colsurfa.2019.03.024

Yang NN, Chen ZG, Zhao ZG, Cui Y (2022) Electrochemical fabrication of ultrafine g-C3N4 quantum dots as a catalyst for the hydrogen evolution reaction. New Carbon Mater 37(2):392-401. https://doi.org/10.1016/S1872-5805(21)60045-8

Yi P, Li Y, Wu XL, Duan X (2024) Z-scheme single-atom photocatalyst for advanced oxidation processes. Curr Opin Chem Eng 45:101028. https://doi.org/10.1016/j.coche.2024.101028

Zhang C, Liu L, Pan Y, Qin R, Wang W, Zhou M, Zhang Y (2025) Detection methodologies and mechanisms of reactive oxygen species generated in Fenton/Fenton-like processes. Sep Purif Technol 355:129578. https://doi.org/10.1016/j.seppur.2024.129578

Zhang J, Jiang X, Wen D, Peng J, Jiang J (2026) Emerging trends of g-C3N4-based photocatalysts from 2020 to 2025. Sci China Mater. https://doi.org/10.1007/s40843-025-4055-6

Zhang Y, Li Y, Huang B, Chen Y, Xu Y, Liu J, Liu K, Zeng Y (2025) Bioinspired fibrous Murray membrane with gradual-transition wettability and pore size for directional water transport and oil/water emulsion separation. Sep Purif Technol 372:133508. https://doi.org/10.1016/j.seppur.2025.133508

Zhang ZH, Wang HJ, Liang YH, Li XJ, Ren LQ, Cui ZQ, Luo C (2018) One-step fabrication of robust superhydrophobic and superoleophilic surfaces with self-cleaning and oil/water separation function. Sci Rep 8(1):3869. https://doi.org/10.1038/s41598-018-22241-9

Zhao G, Wang C, Qi S, Zhang X, Wang X (2026) Recent advances in fluorine-free superhydrophobic textiles: Preparation, applications, and prospects. Prog Org Coat 210:109693. https://doi.org/10.1016/j.porgcoat.2025.109693

Zhao K, Wang Q, Guo F, Kwon M, Li S, Gao W, Chen T, Zan G, Xin B (2026) Robust and multifunctional PDMS/MOF-engineered fabrics with superior water repellency, UV shielding, and EMW absorption. Chem Eng J 538:176610. https://doi.org/10.1016/j.cej.2026.176610

Zhao Q, Zhu Y, Gan Y, Jiang Y, Zhang H, Zhao Y, Dong Q, Chen C (2026) Robust multifunctional protective textiles based on dispersion-enhanced composite coating. Prog Org Coat 216:110136. https://doi.org/10.1016/j.porgcoat.2026.110136

Acknowledgements

The authors would like to acknowledge Erzincan Binali Yıldırım University, Erzincan, Türkiye, and Ondokuz Mayıs University, Samsun, Türkiye. The authors also acknowledge the use of Claude (Anthropic) for language editing, reference formatting and verification, and structural organization of the manuscript.

Author contributions

A.O.Ö.: Conceptualization, methodology, investigation, formal analysis, data curation, visualization, writing—original draft. B.Ç.: Conceptualization, supervision, resources, investigation, writing—review and editing. All authors reviewed the manuscript.

Funding

This research received no external funding.

Data availability

The data that support the findings of this study are available from the corresponding author upon reasonable request.

Declarations

Conflict of interest The authors declare no competing interests.

Ethical approval This study did not involve any humans or animals. Thus, ethical approval was not required.